PHYSICAL REVIEW D **75,** 063512 (2007)

Scale dependence of halo and galaxy bias: Effects in real space

Robert E. Smith*
Department of Physics and Astronomy, University of Pennsylvania, 209 South 33rd Street, Philadelphia, Pennsylvania 19104, USA

Román Scoccimarro†
Center for Cosmology and Particle Physics, Department of Physics, New York University, New York, New York 10003, USA

Ravi K. Sheth‡
Department of Physics and Astronomy, University of Pennsylvania, 209 South 33rd Street, Philadelphia, Pennsylvania 19104, USA
(Received 22 September 2006; published 20 March 2007)

We examine the scale dependence of dark matter halo and galaxy clustering on very large scales ($0.01 < k[h\ \mathrm{Mpc}^{-1}] < 0.15$), due to nonlinear effects from dynamics and halo bias. We pursue a two line offensive: high-resolution numerical simulations are used to establish some old and some new results, and an analytic model is developed to understand their origins. Our simulations show: (i) that the $z = 0$ dark matter power spectrum is suppressed relative to linear theory by $\sim 5\%$ on scales $0.05 < k[h\ \mathrm{Mpc}^{-1}] < 0.075$; (ii) that, indeed, halo bias is *nonlinear* over the scales we probe and that the scale dependence is *a strong function of halo mass*. High mass haloes show no suppression of power on scales $k < 0.07[h\ \mathrm{Mpc}^{-1}]$, and only show amplification on smaller scales, whereas low mass haloes show strong, $\sim 5\%$–10%, suppression over the range $0.05 < k[h\ \mathrm{Mpc}^{-1}] < 0.15$. These results were primarily established through the use of the cross-power spectrum of dark matter and haloes, which circumvents the thorny issue of shot-noise correction. The halo-halo power spectrum, however, is highly sensitive to the shot-noise correction; we show that halo exclusion effects make this *sub-Poissonian* and a new correction is presented. Our results have special relevance for studies of the baryon acoustic oscillation features in the halo power spectra. Nonlinear mode-mode coupling: (i) damps these features on progressively larger scales as halo mass increases; (ii) produces small shifts in the positions of the peaks and troughs which depend on halo mass. We show that these effects on halo clustering are important over the redshift range relevant to such studies ($0 < z < 2$), and so will need to be accounted for when extracting information from precision measurements of galaxy clustering. Our analytic model is described in the language of the ''halo model.'' The halo-halo clustering term is propagated into the nonlinear regime using ''1-loop'' perturbation theory and a nonlinear halo bias model. Galaxies are then inserted into haloes through the halo occupation distribution. We show that, with nonlinear bias parameters derived from simulations, this model produces predictions that are qualitatively in agreement with our numerical results. We then use it to show that the power spectra of red and blue galaxies depend differently on scale, thus underscoring the fact that proper modeling of nonlinear bias parameters will be crucial to derive reliable cosmological constraints. In addition to showing that the bias on very large scales is not simply linear, the model also shows that the halo-halo and halo-dark matter spectra do not measure precisely the same thing. This complicates interpretation of clustering in terms of the stochasticity of bias. However, because the shot-noise correction is nontrivial, evidence for this in the simulations is marginal.

DOI: 10.1103/PhysRevD.75.063512 PACS numbers: 98.80.−k

I. INTRODUCTION

Statistical analysis of the large-scale structures observed in galaxy surveys can provide a wealth of information about the cosmological parameters, the underlying mass distribution, and the initial conditions of the Universe. The information is commonly extracted through measurement of the two-point correlation function [1,2] or its Fourier space analogue the power spectrum [3–7]. When further combined with high precision measurements of the temperature anisotropy spectrum from the cosmic microwave background very strong constraints can be imposed on the initial conditions, the energy content, shape, and evolution of the Universe [8].

For homogeneous and isotropic Gaussian random fields, such as is supposed for the post inflationary density field of cold dark matter (hereafter CDM) fluctuations, each Fourier mode is independent, and thus all of the statistical properties of the field are governed by the power spectrum. However, nonlinear evolution of matter couples the Fourier modes together, and power is transferred from large to small scales [9,10]. Consequently, it is nontrivial to relate the observed structures to the physics of the initial conditions. Further, since one typically measures not the mass, but the galaxy fluctuations, some understanding of the mapping from one to the other is required. This mapping, commonly referred to as galaxy bias, encodes the salient physics of galaxy formation.

*Electronic address: res@astro.upenn.edu
†Electronic address: rs123@nyu.edu
‡Electronic address: shethrk@physics.upenn.edu

One last complication must be added: since galaxy positions are inferred from recession velocities using Hubble's law, and because each galaxy possesses its own peculiar velocity relative to the expansion velocity, a nontrivial distortion is introduced to the clustering on all scales from the velocity field. These velocity effects are commonly referred to as redshift space distortions. Thus one must accurately account for nonlinear evolution of matter fluctuations, bias, and redshift space distortions in order to extract precise information from large-scale structure surveys and this remains one of the grand challenges for modern physical cosmology.

In this paper, we investigate the issue of bias in some detail, through both numerical and analytic means. We focus on real-space effects and reserve our results from redshift space for a subsequent paper. Our numerical work focuses on the generation of multiple realizations of the same cosmological model, in two different box sizes. This allows us to construct halo catalogues spanning a large dynamic range in mass that are largely free from discreteness fluctuations and the multiple realizations allow us to derive errors that are ''true errors from the ensemble.'' We use this data to show that not only is halo clustering on very large scales scale dependent, but that the scale dependence is a strong function of halo mass. These results are completely expected given the standard theoretical understanding of dark matter haloes based on the ''peak-background split'' argument [11–15].

Our analytic approach to modelling these trends can be summarized as follows.

(i) Haloes are biased tracers of the mass distribution. To describe this bias, we assume that the bias relation between the halo density field and the dark matter field is nonlinear, local, and deterministic. This allows us to use the formalism of [13,16]. In order for the local model to hold, one must integrate out small scales where locality is almost certainly violated. This can be done in real space by smoothing small-scale fluctuations, or in Fourier space by considering small wave numbers [17].

(ii) The underlying CDM density field is then propagated into the nonlinear regime using standard Eulerian perturbation theory techniques [10].

(iii) Galaxies are then assumed to form only in haloes above a given mass [18] and these are inserted into each halo using the ''halo-model'' approach [15,19–22].

Because we write the perturbation theory (PT) evolved halo density field as a series expansion we refer to this method as ''halo-PT'' theory.

Our results are particularly relevant for studies which intend to use the baryon acoustic oscillation feature (hereafter BAO) in the low redshift clustering of galaxies to derive constraints on the dark energy equation of state [2]. The CDM transfer function that we have adopted throughout contains a significant amount of BAOs, and we give an accounting of the possible nonlinear corrections from mass evolution and biasing that might influence the detection and interpretation of such features. Previous work in this direction has primarily focused on analysis of numerical simulations [23–27], although several analytic works have recently been presented: [28] derive the exact damping of BAOs in the Zel'dovich approximation and calculate it in the exact dynamics by resumming perturbation theory; [29] consider real-space corrections to the power spectrum from one-loop PT; [30] use the halo model, also in real space, to explore systematics; [31,32] consider a model of Lagrangian displacements fit to simulations.

In Sec. II we discuss how the approach we have developed here is complementary to and expands on these studies. In Sec. III we discuss the numerical simulations and present our measurements of scale dependence in the dark matter, halo center, and halo-dark matter cross-power spectra. We also present the evidence for large-scale nonlinear bias. Then in Sec. IV, we outline some key notions concerning the halo model of large-scale structure, as this is the frame work within which we work. In Sec. IV C we describe the nonlinear bias model that we employ. In Sec. IV D we use the 3rd order Eulerian perturbation theory to describe the evolved Eulerian density field in terms of the initial Lagrangian fluctuations. In Sec. V, we use the 3rd order halo density fields to produce an analytic model for the 1-loop halo and halo-cross dark matter power spectra. In Sec. VI we explore the predictions of the analytic model for a range of different halo masses. In Sec. VII we compare our analytic model to the nonlinear bias seen in the numerical simulations. We use the analytic model to examine the galaxy power spectrum in Sec. VIII, and present our conclusions in Sec. X.

Throughout, we assume a flat Friedmann-Lemaître-Robertson-Walker (FLRW) cosmological model with energy density at late times dominated by a cosmological constant (Λ) and a sea of collisionless cold dark matter particles as the dominant mass density. We take $\Omega_m = 0.27$ and $\Omega_\Lambda = 0.73$, where these are the ratios of the energy density in matter and a cosmological constant to the critical density, respectively. We use a linear theory power spectrum generated from `cmbfast` [33], with baryon content of $\Omega_b = 0.046$ and $h = 0.72$. The normalization of fluctuations is set through $\sigma_8 = 0.9$, which is the initial value of the (root-mean-square) r.m.s. variance of fluctuations in spheres of comoving radius $8h^{-1}$ Mpc extrapolated to $z = 0$ using linear theory.

II. MOTIVATION

A number of recent papers have attempted to quantify the scale dependence of galaxy bias. A subset of these have forwarded simple analytic models to remove the scale-dependent biases in the power spectrum estimator. We

discuss some of these below so as to set the stage for our work.

A. Cole *et al.* (2005)

Based on the analysis of mock galaxy catalogues from the Hubble volume simulation, these authors proposed a simple analytic model to account for the nonlinear scale dependence:

$$P_{\rm gg}(k) = b^2 P_{\rm Lin}(k)\frac{1 + A_2 k^2}{1 + A_1 k}. \quad (1)$$

The parameter $A_1 = 1.4$, and A_2 was allowed to vary over a narrow range, which was then marginalized over in the fitting procedure. When $A_1 k \ll 1$, this model has

$$P_{\rm gg}(k) \approx b^2 P_{\rm Lin}(k)[1 - A_1 k + A_2 k^2]. \quad (2)$$

We show below that the bracketed terms are suggestive of the $P_{13}^{\delta\delta} + P_{22}^{\delta\delta}$ terms from the dark matter perturbation theory, but with incorrect dependence on k. In addition, ignoring the fact that A_1 may depend on galaxy type is a serious inconsistency. For instance, our results indicate that A_1 for luminous red galaxy (LRG)-like galaxies is smaller than 1.4.

A further concern regarding this model is that no accounting for non-Poisson shot noise has been made. If galaxy formation takes place only in haloes, then galaxies are not Poisson samples of the mass distribution. The analytic model we develop shows that it is important to account for this, and how. We are therefore skeptical about the blind use of Eq. (1), particularly with regard to its use in the analysis of LRGs [5,34].

B. Seo and Eisenstein (2005)

These authors examined the scale dependence of halo bias in a large ensemble of low-resolution numerical simulations. They proposed

$$P_{\rm gg}(k) = b^2 P_{\rm Lin}(k) + A_1 k + A_2 k^2 + A_0, \quad (3)$$

which bares some similarity to that of Cole *et al.*, as can be seen by rewriting $A_1 \to A_1/(b^2 P_{\rm Lin})$ and $A_2 \to A_2/(b^2 P_{\rm Lin})$. The effective spectral index of the linear power spectrum evolves from $0 > n_{\rm eff} > -1$ over the range of k of interest, so we can think of $P_{\rm Lin}$ as being approximately constant. Then, the inclusion of the b^2 term decreases the effective A_1 as required, but it also decreases the effective A_2; our results indicate that this is inappropriate.

There is an important difference between this model and the previous one—the inclusion of the constant power term A_0. This was introduced to account for "anomalous power"—by which was meant effects envisaged by [35]—and/or non-Poisson shot noise following [36]. Our analysis strongly supports the inclusion of this term.

C. Seljak (2001); Schulz and White (2006); Guzik, Bernstein, and Smith (2006)

These authors explored the scale dependence of galaxy bias in the halo model focusing their attention on the 1-halo term. They showed that if this was taken simply as a non-Poisson shot-noise correction, then it would be a significant source of scale dependence in the large-scale galaxy power spectrum. We have confirmed this in our study. These studies lead one to suggest a base form of the kind:

$$P_{\rm gg}(k) = b^2 P_{\rm Lin}(k) + A_0. \quad (4)$$

On top of this base form we need to include modifications that capture the true nonlinear evolution of the halo field.

D. Huff *et al.* (2006)

These authors used a set of three large cosmological simulations to investigate the scale dependence of the BAOs. They suggested

$$P_{\rm gg}(k) = b^2 P_{\rm Lin}(k)\exp[-(A_1 k)^2] + A_0, \quad (5)$$

where the exponential damping term was introduced to account for halo profiles. Again examining the large-scale behavior, $A_1 k \ll 1$, we see that this equation may be rewritten

$$P_{\rm gg}(k) \approx b^2 P_{\rm Lin}[1 - (A_1 k)^2] + A_0. \quad (6)$$

If $0 < A_1 < 1$ (the range they considered), then this formula will suppress the power spectrum on scales $k < 0.1h\ {\rm Mpc}^{-1}$ by a percent at most. If this model is to account for the nonlinear corrections that we see, then $A_1 > 1$. However, the strong exponential damping makes it unlikely that this model will properly characterize the transition from the 2- to 1-halo term. This is because, as we show below, the nonlinear evolution of halo centers includes an additional boost at intermediate k which this model does not capture.

E. A necessary model

Our results suggest that a necessary model will have the following properties: the model should be able to produce a previrialization feature and a small-scale nonlinear boost with k-dependencies motivated by physical arguments; nonlinear corrections should depend on galaxy type; a constant power term should be added to account for non-Poisson shot noise. We therefore expect a reasonable starting point for any empirical modelling of the large-scale, scale dependence of the galaxy power spectrum to be

$$P_{\rm gg}(k, T) = b^2(T)[P_{\rm Lin}(k){\rm e}^{-A_1(T)k^2} + A_2(T)k^{m(T)}] \times |W(k/k_\alpha)| + A_0(T)|W(k/k_\beta)| + \frac{1}{\bar{n}_{\rm g}}. \quad (7)$$

Our notation makes explicit that the coefficients have the following properties: $b > 0$, $A_0 > 0$, $A_1 > 0$, $A_2 > 0$, and

$m \geq 0$, and that all depend on galaxy type T. The first term is composed of two pieces: in the first piece, we have modeled the damping of BAOs using a Gaussian as derived in [37,38] for the dark matter case; for the second piece, we have added a k-dependent boost that models the power added by mode-mode coupling and nonlinear bias. Our simple power-law form (with two parameters A_2, m) is meant to describe this effect over a restricted range of scales. The fact that this term is additive as opposed to multiplicative, is meant to emulate the fact that in PT this corresponds to the $P_{22}^{\delta\delta}$ term which arises from the convolution of linear power on different scales and is therefore smooth possessing no information on BAOs. For weakly nonlinear scales it has a positive spectral index (note, however, that in the limit $k \longrightarrow 0$, $m = 4$ is expected from momentum conservation arguments). The second term corresponds to Poisson shot noise from unequal weighting of haloes. The last term corresponds to the Poisson shot noise from the galaxy point distribution. We have included filter terms $W(k/k_\alpha)$ and $W(k/k_\beta)$ to indicate the damping due to density profiles, which will occur for $k > 1/r_{\rm vir}$. This function may be greatly simplified by examining the case $k \ll 1[h\ {\rm Mpc}^{-1}]$, for which it reduces to

$$P_{\rm gg}(k,T) = b^2(T)\{P_{\rm Lin}[1 - A_1(T)k^2] + A_2(T)k^{m(T)}\} + \tilde{A}_0(T), \qquad (k \ll 1), \tag{8}$$

where the parameter $\tilde{A}_0(T)$ subsumes all sources of constant large-scale power.

III. SCALE-DEPENDENT HALO BIAS FROM NUMERICAL SIMULATIONS

A. Simulation details and halo catalogues

We have performed a series of high-resolution, collisionless dark matter N-body simulations, where $N = 512^3$ equal mass particles. Each simulation was performed using `Gadget2` [39]; the internal parameter settings can be found in Table 1 of [40], where more details about the runs themselves are available. The initial conditions were set up using the 2nd-order Lagrangian perturbation theory at redshift $z = 49$ [40], with linear theory power spectrum taken from `cmbfast` [33], with the cosmological model being the same as that used throughout this paper. We will present results from two different box sizes: 20 smaller higher resolutions box (hereafter HR) for which the volume is $V = L^3 = (512h^{-1}\ {\rm Mpc})^3$, and 8 realizations of a larger, lower resolution box (hereafter LR) for which $L = 1024h^{-1}$ Mpc box.

Haloes were identified in the $z = 0$ outputs using the friends-of-friends algorithm with linking-length parameter $l = 0.2$. Halo masses were corrected for the error introduced by discretization of the halo density structure [41]. Since the error in the estimate of the halo mass diverges as the number of particles sampling the density field decreases, we only study haloes containing 50 particles or more. For the HR and LR simulations this corresponds to haloes with $M > 4.0 \times 10^{12}h^{-1}M_\odot$ and $M > 4.0 \times 10^{13}h^{-1}M_\odot$, respectively. We then constructed four nonoverlapping subsamples of haloes with roughly equal numbers per subsample. The two low mass bins were harvested from the HR simulations and the two high mass ones were taken from the LR runs. Further details may be found in Table I.

B. Mass, halo, and halo-mass power spectra

For each realization and each bin in halo mass we measured the following quantities: the power spectrum of the dark matter $P^{\delta\delta}(k)$; the power spectrum of dark matter haloes $P^{\rm hh}(k)$; and the cross-power spectrum of dark matter and dark matter haloes, $P^{\delta{\rm h}}(k)$. The power spectra may be generally defined

$$\langle \delta^\alpha(\mathbf{k})\delta^\beta(\mathbf{k}')\rangle \equiv (2\pi)^3\delta^D(\mathbf{k}+\mathbf{k}')P^{\alpha\beta}(k), \tag{9}$$

where

$$\delta^i(\mathbf{k}) \equiv \begin{bmatrix} \delta(\mathbf{k}) \\ \delta^{\rm h}(\mathbf{k}) \end{bmatrix}; \qquad P^{ij}(k) \equiv \begin{bmatrix} P^{\delta\delta}(k) & P^{\delta{\rm h}}(k) \\ P^{{\rm h}\delta}(k) & P^{\rm hh}(k) \end{bmatrix}, \tag{10}$$

with $\delta(\mathbf{k})$ and $\delta^{\rm h}(\mathbf{k})$ being the Fourier transforms of the mass and halo density perturbation fields,

$$\rho^i(\mathbf{x}) = \bar{\rho}^i[1 + \delta^i(\mathbf{x})], \tag{11}$$

where the index i again distinguishes between dark matter and haloes, e.g. $\bar{\rho}^1 \equiv \bar{\rho}$ and $\bar{\rho}^2 \equiv \rho^{\rm h}$.

We estimate the spectra through the conventional fast fourier transform (FFT) method [42] (for a detailed discussion see [43]). The mean power and 1-σ errors on the spectra were estimated from the ensemble neglecting the bin-to-bin covariances. Inspection of an estimate of the covariance matrix from the 20 HR simulations showed that this is reasonable. There is, however, a small degree of off diagonal covariance, but the number of simulations was insufficient to make a precise estimate.

Figure 1 shows the three types of power spectra measured from the ensemble of simulations for each of the four

TABLE I. Halo samples. $N_{\rm real}$ is the number of independent realizations. $\bar{N}_{\rm h}$ and $\bar{n}_{\rm h}$ are the ensemble average number and number densities of haloes in each mass bin.

		$N_{\rm real}$	L [Mpch^{-1}]	$\bar{N}_{\rm h}$ [$\times 10^4$]	$\bar{n}_{\rm h}$ [Mpc$^{-3}h^3$]
LR	Bin 1[a]	8	1024	3.6863	$3.433\,13 \times 10^{-5}$
LR	Bin 2[b]	8	1024	7.3530	6.8480×10^{-5}
HR	Bin 3[c]	20	512	6.9287	5.1623×10^{-4}
HR	Bin 4[d]	20	512	5.5415	4.1287×10^{-4}

[a]Mass bin $1 = M > 1.0 \times 10^{14}h^{-1}M_\odot$
[b]Mass bin $2 = 1.0 \times 10^{14}h^{-1}M_\odot > M > 4.0 \times 10^{13}h^{-1}M_\odot$
[c]Mass bin $3 = 4.0 \times 10^{13}h^{-1}M_\odot > M > 7.0 \times 10^{12}h^{-1}M_\odot$
[d]Mass bin $4 = 7.0 \times 10^{12}h^{-1}M_\odot > M > 4.0 \times 10^{12}h^{-1}M_\odot$

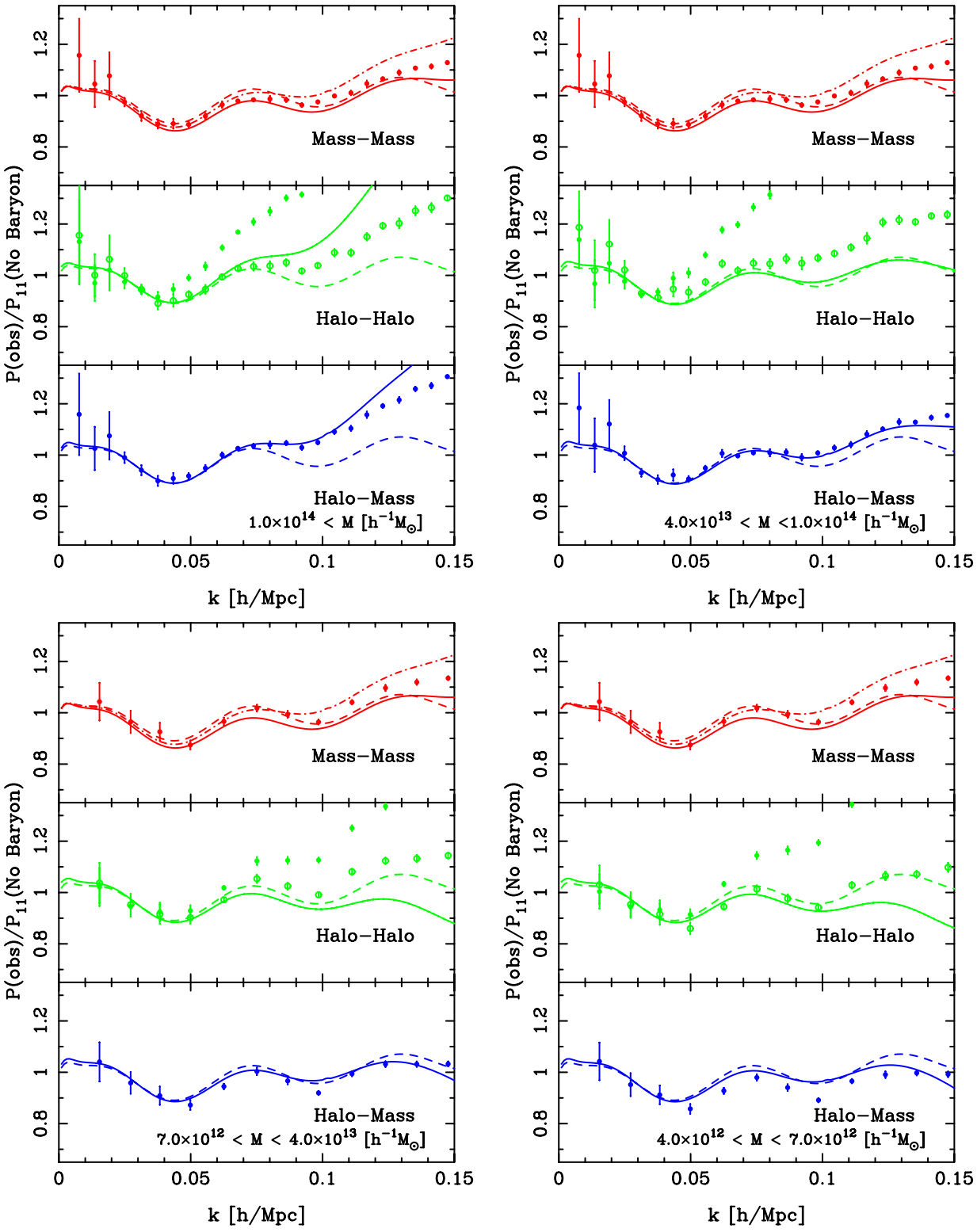

FIG. 1 (color online). Halo power spectrum measurements and predictions, ratioed with a smooth "No-Baryon" dark matter power spectrum, for four bins in halo mass: results for massive haloes (the top two panels) are from the LR simulations, whereas lower masses (the two bottom panels) are from the HR simulations. Filled circles in the top, middle, and bottom sections of each panel show the ensemble average nonlinear $P^{\delta\delta}(k)$ $P^{\rm hh}(k)$, and $P^{\delta{\rm h}}$, respectively. The open circles in the middle sections show $P^{\rm hh}(k)$ with the nonstandard shot-noise subtraction described in Appendix A. In all panels the linear theory dark matter, halo-halo, and halo cross-power spectra are shown as dashed lines. The top panel also shows predictions from `halofit` (solid lines) [43] and 1-loop perturbation theory (dot-dashed lines). Solid lines in the middle and bottom panels show our new analytic model, halo-PT.

bins in halo mass described in Table I. The filled circles and associated error bars in the top, middle, and bottom sections of each panel show $\hat{P}^{\delta\delta}(k)$, $\hat{P}^{\rm hh}(k|M)$, and $\hat{P}^{\delta{\rm h}}(k|M)$. The open circles show the result of applying a nonstandard shot-noise correction to $\hat{P}^{\rm hh}$, which we describe in Appendix A.

To emphasize the nonlinear evolution of the spectra and the BAOs, in particular, we have divided each spectrum by a smooth linear theory spectrum, which we shall refer to as our "No-Baryon" model. This was constructed by performing a chi-squared fit of the `cmbfast` transfer function data to the smooth transfer function model of [44],

$$T(k) = [1 + \{aq + (bq)^{1.5} + (cq)^2\}^d]^{-1/d}. \quad (12)$$

The derived parameters are: $q = k/0.19$, $a = 4.86$, $b = 4.81$, $c = 1.72$, $d = 1.18$.

To compare the halo spectra with the linear theory we require estimates of the halo bias on very large scales, which we measure as follows. We begin by assuming that the spectra can be written

$$P^{ij}(k|M) = \mathcal{A}^{ij} P_{\rm Lin}(k); \qquad \mathcal{A}^{ij} = \begin{bmatrix} 1 & b^{{\rm h}\delta} \\ b^{\delta{\rm h}} & (b^{\rm hh})^2 \end{bmatrix}, \quad (13)$$

where i and j denote the type of spectrum considered and where, for reasons that will later be apparent, we distinguish between the bias from $P^{\delta{\rm h}}$ and $P^{\rm hh}$. Hence, the likelihood of obtaining an estimate of the power $\hat{P}^{ij}$ in the lth k-bin is assumed to be an independent Gaussian with dispersion σ_i

$$\mathcal{L}(\hat{P}_l^{ij}, \sigma_l | \mathcal{A}, P_{\rm Lin}) = \frac{1}{\sqrt{2\pi}\sigma_l} \exp\left\{-\frac{[\hat{P}_l^{ij} - \mathcal{A} P_{\rm Lin}(k_l)]^2}{2\sigma_l^2}\right\}. \quad (14)$$

Thus the combined likelihood of obtaining the data set $\{\hat{P}_l^{ij}, \sigma_l\}$ can be written

$$\mathcal{L}(\{\hat{P}_l^{ij}\}, \{\sigma_l\} | \mathcal{A}, P_{\rm Lin}) = \prod_{l=1}^{N_{\rm dat}} \mathcal{L}(\hat{P}_i^{ij}, \sigma_l | \mathcal{A}, P_{\rm Lin}). \quad (15)$$

On maximizing the likelihood function, we find the following estimator for the halo bias matrix

$$\hat{\mathcal{A}} = \frac{\sum_{l=1}^{N_{\rm dat}} P_{\rm Lin}(k_l) \hat{P}_l^{ij}/\sigma_l^2}{\sum_{l=1}^{N_{\rm dat}} [P_{\rm Lin}(k_l)/\sigma_l]^2}. \quad (16)$$

We construct error estimates through further differentiation of the Gaussian likelihood function:

$$\sigma_{\mathcal{A}} = \left(\frac{\partial^2 \log \mathcal{L}}{\partial \mathcal{A}^2}\right)^{-1/2} = \left(\sum_{i=1}^{N_{\rm dat}} \left[\frac{P_{\rm Lin}(k_i)}{\sigma_i}\right]^2\right)^{-1/2}. \quad (17)$$

Lastly, since we observe scale-dependent nonlinear effects in the matter power spectrum for $k > 0.05h$ Mpc^{-1}, we only use modes with $k < 0.04h$ Mpc^{-1} in the fitting of the amplitude matrix $\mathcal{A}$. Estimates of the large-scale bias parameters $b^{\rm hh}$ and $b^{\delta{\rm h}}$ are presented in Table II [45].

TABLE II. Bias parameters for the halo samples. $b_1^{\rm ST}$, $b_2^{\rm ST}$, and $b_3^{\rm ST}$ are the first three nonlinear halo bias parameters derived from the Sheth and Tormen model [14,15] averaged over halo bins. b_1^δ, b_2^δ, and b_3^δ are the parameters measured from the $\delta^{\rm h}$-δ scatter plots. $b^{\delta{\rm h}}$ is the large-scale bias parameter measured directly from $P^{\delta{\rm h}}$.

	$b^{\delta{\rm h}}$	$b_1^{\rm ST}$	$b_2^{\rm ST}$	$b_3^{\rm ST}$	b_1^δ	b_2^δ	b_3^δ
Bin 1[a]	2.28 ± 0.03	2.19	0.94	−0.98	2.23	1.68	−4.08
Bin 2	1.49 ± 0.04	1.53	−0.30	0.94	1.41	0.04	−1.29
Bin 3	1.02 ± 0.03	1.13	−0.46	1.47	1.04	−0.85	0.37
Bin 4	0.87 ± 0.03	0.98	−0.44	1.44	0.91	−0.74	0.55

[a]See Table I for definition of bins.

The dark matter power spectra in Fig. 1 show significant deviations away from the linear theory prediction: at $0.05 < k[h\ {\rm Mpc}^{-1}] < 0.075$, there is a suppression of power relative to linear theory, whereas at $k > 0.075[h\ {\rm Mpc}^{-1}]$ there is an amplification. Perturbation theory studies [10] refer to the suppression effect (caused by tidal terms) as previrialization. Recently, this has been understood in much more detail as a result of the damping of linear features by nonlinearities, leading to an exponentially decaying propagator that measures the loss of memory of the density field to the initial conditions [37,38]. Although the effect in the power is rather well known and has been observed in recent numerical simulations of CDM spectra [4,43,46,47], our results constitute a rather precise measurement of this effect, with realistic errors drawn from the ensemble. A complete assessment of the damping of linear features such as BAOs is done by studying the propagator [37,38] rather than the power spectrum. See [28] for further discussion on this.

The solid and dot-dashed lines show predictions based on `halofit` [43] and on 1-loop PT. The PT results do well compared to the simulations on very large scales, but for $k > 0.07$ they increasingly overpredict the power. We note also that PT appears to predict the previrialization feature in the simulations, adding additional support to the claim that $\hat{P}^{\delta\delta}(k)$ requires nonlinear corrections on the scales of interest. However, qualitatively, it underpredicts the magnitude of the effect. We note that `halofit` does reasonably well at capturing the behavior for $k < 0.07h$ Mpc^{-1}, but it appears to underpredict the measured data.

Before moving on to $P^{\rm hh}$ and $P^{\delta{\rm h}}$, we think it is worth noting that the BAOs in $P^{\delta\delta}$ on $k > 0.1h$ Mpc^{-1} have been erased. The large-box LR measurements show that the third peak is gone, and the height of the second peak has dropped so that it appears more as a plateau. However, the behavior at $k < 0.05h$ Mpc^{-1} appears unchanged.

Discreteness corrections for $P^{\delta\delta}(k)$ have been studied in some depth [43]. However, for $P^{\rm hh}$, the appropriate correction is more complicated because haloes are rare, highly clustered, and spatially exclusive. In Appendix A we show

that the standard Poisson shot-noise correction for the cluster power spectrum results in *negative power* at high k. This lead us to propose a new method for making the shot-noise correction that accounts for exclusion, which we discuss therein. The open circles in the middle sections of each panel in Fig. 1 show the result of this new correction. Filled circles show the uncorrected power, and stars show the standard correction—clearly, the choice of correction is crucial. Note that owing to the arbitrary normalization things for the standard shot-noise method look better than they actually are. Unfortunately, the residual uncertainties in our new procedure prevent us from making strong statements about the scale dependence of halo-halo clustering.

Whilst the discreteness correction is troublesome for $P^{\rm hh}$ it is almost negligible for $P^{\delta{\rm h}}$ (the halo-model arguments which follow allow us to quantify this). Our estimates of $P^{\delta{\rm h}}$ are shown in the bottom sections of the panels in Fig. 1. Notice that the scale dependence of $P^{\delta{\rm h}}$, is a strong function of halo mass. $P^{\delta{\rm h}}$ for the most massive haloes shows no deviations from linear theory until $k > 0.7h$ Mpc^{-1}. However, the previrialization feature appears and gets enhanced as one goes to lower masses. Indeed, for our lowest mass bin, $P^{\delta{\rm h}}$ is sublinear until $k > 0.15h$ Mpc^{-1}.

This has important consequences for the BAOs. In the highest mass bin (top-left panel), the oscillations in $P^{\delta{\rm h}}$ at $k > 0.07h$ Mpc^{-1} have been erased. However, the first trough, at $k \sim 0.04h$ Mpc^{-1}, is unaffected. For the next mass bin (top-right panel), the first peak and trough are unmodified, and the second peak is becoming noticeable. This trend continues as we decrease mass; there is even a hint of the third peak in the bottom panels. These measurements indicate that nonlinear dynamics can erase oscillations on progressively larger scales as halo mass increases and small displacements to the positions of the peaks and troughs may occur; these will also be dependent on halo mass. If the locations of these peaks and troughs are to play an important role in constraining cosmological parameters, our measurements suggest that understanding and quantifying these displacements will be very important.

Before continuing, we comment on the possible explanation of these shifts through simple scatter from cosmic variance. We remark that it is certainly possible to reconcile some of the shifts in the peak positions through this. However, we draw attention to the fact that all of the points $k \geq 0.05$ in the cross-power spectra of the low mass haloes are systematically lower than expected from the linear theory. We also reiterate that the derived error bars are the errors on the means for 20 realizations. One caveat is that since the spectra are normalized by the very large-scale modes of the power spectrum, where cosmic variance errors are larger, we expect some small fluctuations in the relative amplitudes of the theory predictions as more data is acquired. Estimates of the error in the present LR simulations suggest changes of the order $\sim 1\%$ to be acceptable; and this increases to $\sim 3\%$ for the HR simulations. If the amplitudes for the theory curves are too low by $\sim 3\%$, then some of these discrepancies may be alleviated. However, it is unquestionable that nonlinear effects are present on these scales and we must therefore firmly accept that it is likely that these may cause some shifting of the harmonic series. Only a wider and expanded numerical study will be able to address and answer these questions more completely.

The solid lines in the middle and bottom sections of each panel show predictions from the analytic model described in the following sections. In all cases this model provides a better description than does linear theory.

C. Scale dependence of the bias

Next, we examine the scale dependence of halo bias. We will consider

$$\hat{b}^{\rm hh}_{\rm NL}(k_i) = \sqrt{\frac{\hat{P}^{\rm hh}(k_i)}{\hat{P}^{\delta\delta}(k_i)}}; \qquad \hat{b}^{\delta{\rm h}}_{\rm NL}(k_i) = \frac{\hat{P}^{\delta{\rm h}}(k_i)}{\hat{P}^{\delta\delta}(k_i)}, \tag{18}$$

as well as

$$\hat{b}^{\rm hh}_{\rm Lin}(k_i) = \sqrt{\frac{\hat{P}^{\rm hh}(k_i)}{P_{\rm Lin}(k_i)}}; \qquad \hat{b}^{\delta{\rm h}}_{\rm Lin}(k_i) = \frac{\hat{P}^{\delta{\rm h}}(k_i)}{P_{\rm Lin}(k_i)}. \tag{19}$$

For any particular realization the wave modes of the halo and dark matter density fields are almost perfectly correlated. Because the first set of estimators are derived from taking the ratio of measured power spectra, they are insensitive to this source of cosmic variance. In this sense, the second set of estimators are nonoptimal. However, they are the ones which will be used with real data, since $P^{\delta\delta}$ is generally not observable.

In Fig. 2 we show the results of measuring these quantities for the same halo-mass bins as in the previous section. The top and bottom parts of each panel show (18) and (19), respectively. The error bars, which were derived from the ensemble to ensemble variations, are significantly larger for (19) than for (18), as expected. The solid lines show the predictions from the new analytic model described in the next section.

For $b^{\rm hh}$ we show both the shot-noise corrected (large stars) and uncorrected (small stars) results. As was the case for the halo-halo power spectra, we see that this correction is important, so it must be known rather accurately. The estimators for $b^{\delta{\rm h}}$ are also shown (filled circles). Except for the highest mass bin, $b^{\rm hh} \geq b^{\delta{\rm h}}$. Indeed, as we shall argue later, there are compelling theoretical reasons why the biases derived from $P^{\delta{\rm h}}$ and $P^{\rm hh}$ are not in fact the same, and that, one generally expects $b^{\rm hh} \geq b^{\delta{\rm h}}$. However owing to the uncertainty regarding the shot-noise correction, no firm statement can be drawn from the current data.

Two possible explanations why the highest mass halo bin appears to behave differently are: First, if the shot-

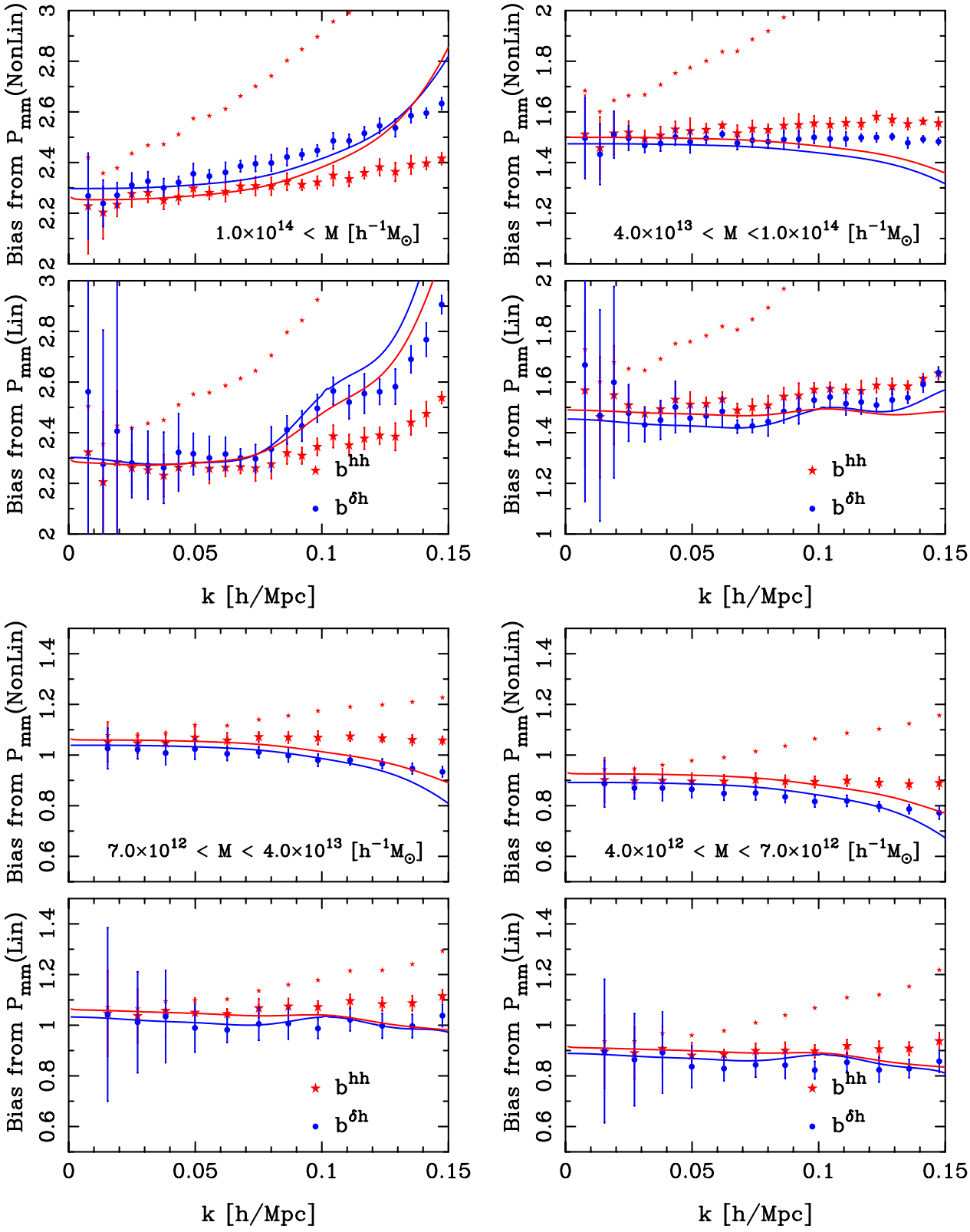

FIG. 2 (color online). Large scale halo bias derived directly from N-body simulations for four bins in halo mass. The top sections of each panel show the estimators $\hat{b}^{\delta h}_{\rm NL}$ (solid points) and $\hat{b}^{\rm hh}_{\rm NL}$ with and without shot-noise correction (large and small stars, respectively). The bottom panels show the same, but for $\hat{b}^{\delta h}_{\rm Lin}$ and $\hat{b}^{\rm hh}_{\rm Lin}$ (See Eqs. (18) and (19) for definitions). The solid lines in each panel show the predictions for the bias from our halo-PT model.

noise correction to $P^{\rm hh}$ is too aggressive, we may have underestimated the true $P^{\rm hh}$ and therefore the bias. Alternatively, we have made no shot-noise correction to $P^{\delta{\rm h}}$; if one should be applied (we think this is unlikely, owing to the large number of dark matter particles), then our current estimate of $b^{\delta{\rm h}}$ may be biased high.

The estimators based on Eq. (19) show more scale dependence than those based on (18), especially for the two high mass bins. As noted by [30], this is because the BAOs are erased on larger and larger scales as higher and higher mass haloes are considered. Thus on dividing the halo spectra by a linear theory BAO spectrum, we are in fact introducing scale dependence from the linear model.

For the highest mass haloes, $\hat{b}^{\delta{\rm h}}_{\rm NL}$ is constant at $k < 0.04h$ Mpc^{-1}, but it increases monotonically as k increases. This is a direct consequence of the absence of previrialization in $P^{\rm hh}$ on intermediate scales and the rapid onset of nonlinear power on smaller scales, compared to $P^{\delta\delta}$. The bias $\hat{b}^{\delta{\rm h}}_{\rm NL}$ is flat for haloes with masses $(4.0 \times 10^{13} < M[h^{-1}M_\odot] < 1.0 \times 10^{14})$, suggesting that small clusters and group mass haloes are linearly biased tracers of the nonlinear dark matter. The smallest two bins in halo mass show the reverse trend: the bias decreases at large k, by $\sim$10% compared to the approximately constant value at smaller k.

IV. THEORETICAL MODEL

We now describe a model for interpreting the trends seen in the previous section. Our discussion is based on the halo model, which we briefly summarize below. See [48] for a more detailed review.

A. The halo model of large-scale structure

The halo model may be described by the simple statement:

(i) All dark matter in the Universe is contained within a distribution of CDM haloes, with masses drawn from some mass function and with the density profile of each halo being drawn from some universal stochastic profile.

The model attains its full potential when the second assumption is stated:

(i) All galaxies exist only in isolated dark matter haloes, with more massive haloes hosting multiple galaxies.

In essence the model has been in existence for several decades [12,18,49–53]. However it was not until the advent of large numerical N-body simulations and accurate characterization of halo phenomenology that its true value was realized. Namely, given an appropriate halo occupation distribution (HOD—i.e., a prescription for the number and spatial distribution of galaxies within a halo) the model successfully reproduces the real-space form of the two-point correlation function of galaxies over a wide range of scales. It predicts subtle deviations from a power-law which have recently been seen in observations [54] and provides a framework for describing the luminosity [55,56] and environmental dependence of galaxy clustering [57,58]. It also enables new tests of the CDM paradigm to be constructed [59,60].

B. Power spectra

In the model the density fields of haloes and dark matter may be written as a sum over haloes,

$$\rho^i(\mathbf{x}) \equiv \bar{\rho}^i[1 + \delta^i(\mathbf{x})] = \sum_j^{N_i} M_j U_j(\mathbf{x} - \mathbf{x}_j|M_j), \quad (20)$$

where $i = \{1, 2\}$ distinguishes between haloes and dark matter and $N_1 = N$ and $N_2 = N_{\rm h}$ are the total number of haloes and the number of haloes in some restricted range in mass. M_j and $\mathbf{x}_j$ are the mass and center of mass of the jth halo and $U_j \equiv \rho_j(\mathbf{x}_j)/M_j$ is the mass normalized density profile. Following [52], the power spectra $P^{\delta\delta}$, $P^{\delta{\rm h}}$, and $P^{\rm hh}$ can be written as the sum of two terms:

$$P^{ij}(\mathbf{k}) = P^{ij}_{\rm 1H}(\mathbf{k}) + P^{ij}_{\rm 2H}(\mathbf{k}). \quad (21)$$

The first term, $P^{ij}_{\rm 1H}$, referred to as the 1-halo term, describes the intraclustering of dark matter particles within single haloes; the second, $P^{ij}_{\rm 2H}$, referred to as the 2-halo term, describes the clustering of particles in distinct haloes. They have the explicit forms:

$$P^{ij}_{\rm 1H}(\mathbf{k}) = \frac{1}{\bar{\rho}^i\bar{\rho}^j}\int_0^\infty dM n(M)M^2|U(\mathbf{k}|M)|^2 \times \Theta_{ij}(M, M); \quad (22)$$

$$P^{ij}_{\rm 2H}(\mathbf{k}) = \frac{1}{\bar{\rho}^i\bar{\rho}^j}\int_0^\infty \prod_{l=1}^{2}\{dM_l n(M_l)M_l U_l(\mathbf{k}|M_l)\}P^{\rm hh}_{\rm c}(\mathbf{k}|M_1, M_2)\Theta_{ij}(M_1, M_2), \quad (23)$$

where $n(M)$ is the halo-mass function, which gives the number density of haloes with masses in the range M to $M + dM$, per unit mass. The θ_{ij} matrix carves out the halo density field to be considered, e.g. for haloes with mass $M > M_{\rm cut}$ the matrix is

$$\Theta_{ij}(M_1, M_2) \equiv \begin{bmatrix} \Theta(M_1)\Theta(M_2) & \Theta(M_1)\Theta(M_2 - M_{\rm cut}) \\ \Theta(M_1 - M_{\rm cut})\Theta(M_2) & \Theta(M_1 - M_{\rm cut})\Theta(M_2 - M_{\rm cut}) \end{bmatrix},$$

where $\Theta(x)$ is the Heaviside step function. More complicated halo selections can easily be described through the Θ_{ij} notation. Lastly, $P^{\rm hh}_{\rm c}(\mathbf{k}|M_1, M_2)$ is the power spectrum of halo centers with masses M_1 and M_2. This function contains all of

the information for the interclustering of haloes; precise knowledge of this term is required to make accurate predictions on large scales.

In principle, $P_c^{hh}(\mathbf{k}|M_1, M_2)$ is a complicated function of M_1, M_2, and $\mathbf{k}$. Initial formulations of the halo model [15,20,21,61] assumed that it could be well approximated by

$$P_c^{hh}(k|M_1, M_2) = b_1(M_1)b_1(M_2)P_{Lin}(k), \qquad (24)$$

where all the scale dependence is in $P_{Lin}(k)$, which is taken from linear theory, and all the mass dependence is in the scale-independent bias parameter $b_1(M)$ [12,14]. In this approximation, $P_c^{hh}(\mathbf{k}|M_1, M_2)$ is a separable function of M_1, M_2, and $\mathbf{k}$. As we show below, comparison with numerical simulations shows that this simple model overpredicts power on very large scales and provides insufficient power on intermediate scales. In both cases, this is about a 10% effect.

This discrepancy is not unexpected [22,62,63]. A simple correction results from setting

$$P_c^{hh}(k|M_1, M_2) = b_1(M_1)b_1(M_2)P_{NL}(k), \qquad (25)$$

where P_{NL} is the nonlinear rather than the linear matter power spectrum, and, in addition, imposing an exclusion constraint:

$$\xi_c^{hh}(r|M_1, M_2) = -1; \qquad (r < r_{vir_1} + r_{vir_2}), \qquad (26)$$

where r_{vir} is the virial radius of the halo.

The success of this approach is demonstrated by comparing $P^{\delta\delta}(k)$ measured in the $z = 0$ output of the Hubble volume simulation [64] with the halo-model calculation. The open and filled symbols in the top panel of Fig. 3 show the measurement before and after subtracting a Poisson shot-noise term (which is shown by the triple dot-dashed line.) The dot-short dash line shows the linear theory prediction, and the other two dot-dashed curves show two estimates of the 2-halo term: the one which drops more sharply at large k is based on Eq. (25) and the other one is based on the original approximation of Eq. (24). Since Eq. (25) requires the use of a nonlinear power spectrum, we used the one provided by [43].

The symbols in the bottom panel show the measurements divided by the halo-model calculation which uses Eq. (24) for the 2-halo term (i.e. the initial linear theory-based approximation). Notice how they drop below unity at $k \sim 0.1h$ Mpc^{-1}. The solid line shows the halo-model calculation which is based on Eq. (25)—it reproduces this previrialization feature well.

As an interesting aside, we note that the fitting formula `halofit` does very well at matching the previrialization feature. Whilst it is not apparent from the figure we also point out that the transfer function of the Hubble volume simulation does contain BAOs; thus, our results demonstrate that the fitting formula of [43] appears to be accurate, for this data, for BAO models to roughly ~5%. In light of this, we note that the discrepancy between `halofit` and the mass power spectra from our smaller box HR simulations is somewhat puzzling. We highlight this issue for further study, one possible explanation is the difference in initial power spectra, on the other hand, also note that a calculation within the framework of renormalized perturbation theory [37] suggests that even for these simulation volumes one expects small effects due to the absence of coupling to large scales.

To fix the small discrepancies which remain, some authors have advocated making the halo bias factors scale dependent [65], but the implementation has been based on fitting formulae rather than fundamental theory. While

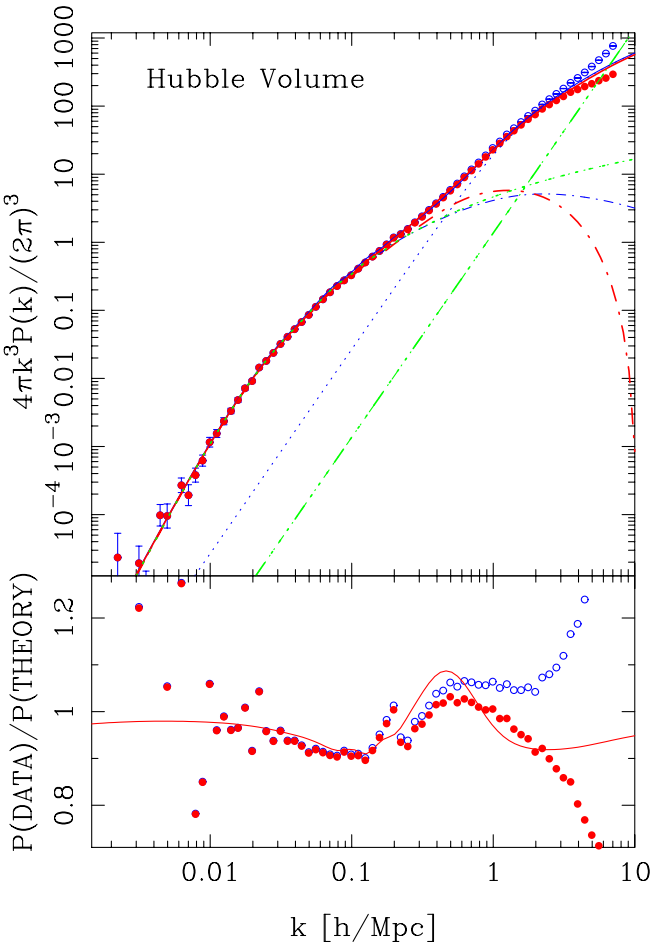

FIG. 3 (color online). Dark matter power spectrum measured as a function of wave number measured from the $z = 0$ time slice of the Hubble volume simulation [64]. In the top panel the points show the estimates of the dark matter power spectrum measured from the simulation, with and without a Poisson shot-noise correction. The dot-dashed line shows the linear theory and the triple dot-dashed line shows the Poisson correction. The dotted and dot-dashed curves show the 1- and 2-halo terms. The thick dot-dashed curve shows the 2-halo term where P_{NL} has been used instead of P_{Lin}. The bottom panel presents the ratio with respect to the halo model, but with Eq. (24) for the 2-halo term. The solid line shows the effect of the P_{NL} modification.

Eq. (25) appears to fare better than the original approximation (24), as we will soon show, in going from (24) to (25), one is making the assumption that halo bias is linear even when the mass density field is not. If this is not the case then the method is incorrect. In addition, there is an unpleasant circularity in requiring prior knowledge of $P_{\rm NL}(k)$ in order to predict $P_{\rm NL}(k)$.

C. Halo bias: The nonlinear local bias model

The discussion above makes clear that a rigorous treatment of the 2-halo term is currently lacking. This term requires a description of how dark matter haloes cluster. Whereas current models seek to describe halo clustering as a biased version of dark matter clustering, the scale dependence of halo bias is still rather poorly understood [11–14,65–72]. In the following sections we develop a model to understand its main properties. In particular, we will discuss a general nonlinear, deterministic, local bias model for dark matter haloes. This model is exactly analogous to that derived for galaxy biasing by [16] and first applied to dark matter haloes by [13].

To begin, consider the density field of all haloes with masses in the range M to $M + dM$, smoothed with some filter of scale R. We now assume that this field can be related to the underlying dark matter field, smoothed with the same filter, through some deterministic mapping and that this mapping should apply independently of the precise position, $\mathbf{x}$, in the field: i.e.

$$\delta^{\rm h}(\mathbf{x}|R, M) = \mathcal{F}_{\{M,R\}}[\delta(\mathbf{x}|R)], \tag{27}$$

where the subscripts on the function $\mathcal{F}$ indicate that it depends on the mass of the haloes considered and the chosen filter scale. The filtered density field is

$$\delta(\mathbf{x}|R) = \frac{1}{V}\int d^3y\,\delta(\mathbf{y})W(|\mathbf{x}-\mathbf{y}|, R), \tag{28}$$

$W(|x|, R)$ being some normalized filter. Taylor expanding $\mathcal{F}_{\{M,R\}}$ about the point $\delta = 0$ yields

$$\mathcal{F}_{\{M,R\}}[\delta(\mathbf{x}|R)] = \sum_i \frac{b_i(M|R)}{i!}[\delta(\mathbf{x}|R)]^i. \tag{29}$$

We now assume that there is a certain filter scale above which $\mathcal{F}_{\{M,R\}}$ is independent of both the scale considered and also the exact shape of the filter function. Hence,

$$\delta^{\rm h}(x|R, M) = \sum_{i=0}^{\infty}\frac{b_i(M)}{i!}[\delta(\mathbf{x}|R)]^i, \tag{30}$$

where the bias coefficients are

$$b_i(M) \equiv \frac{\partial^i \mathcal{F}_{\{M\}}[\chi]}{\partial\chi^i}\bigg|_{\chi=0}. \tag{31}$$

The linear bias model has $b_i = 0$ for all $i > 1$.

The bias coefficients from the Taylor series are not independent, but obey two constraints. The first arises from the fact that $\langle\delta^{\rm h}(\mathbf{x}|R)\rangle = 0$, which leads to

$$b_0 = -\frac{b_2}{2}\langle\delta^2\rangle - \frac{b_3}{3!}\langle\delta^3\rangle - \cdots - \frac{b_n}{n!}\langle\delta^n\rangle. \tag{32}$$

Thus, in general b_0 is nonvanishing and depends on the hierarchy of moments. This allows us to rewrite Eq. (30) as

$$\delta^{\rm h}(x|R, M) = \sum_{i=1}^{\infty}\frac{b_i(M)}{i!}\{[\delta(\mathbf{x}|R)]^i - \langle\delta^i(\mathbf{x}|R)\rangle\}. \tag{33}$$

Nevertheless, we may remove b_0 from further consideration by transforming to the Fourier domain, where it only contributes to $\delta(\mathbf{k} = 0)$.

The second constraint states that a sum over all halo density fields $\delta^{\rm h}(x|M)$ weighted by halo mass and abundance must recover the dark matter density field [15]. This requires that

$$\frac{1}{\bar\rho}\int dMn(M)Mb_i(M) = \begin{cases}1 & (i=1)\\ 0 & (i=0,2,3,\ldots)\end{cases}. \tag{34}$$

For CDM models whose initial density perturbations are Gaussian random, the bias coefficients may either be derived directly through the "peak-background split" argument [11–14] or measured directly from N-body simulations. Figure 4 shows the halo bias parameters up to third order, derived in the context of the Sheth-Tormen mass function; see [15] for the analytic expressions. We compare these with measurements from our simulations in Appendix B.

A practical application of this method rests squarely upon our ability to truncate the Taylor series at some

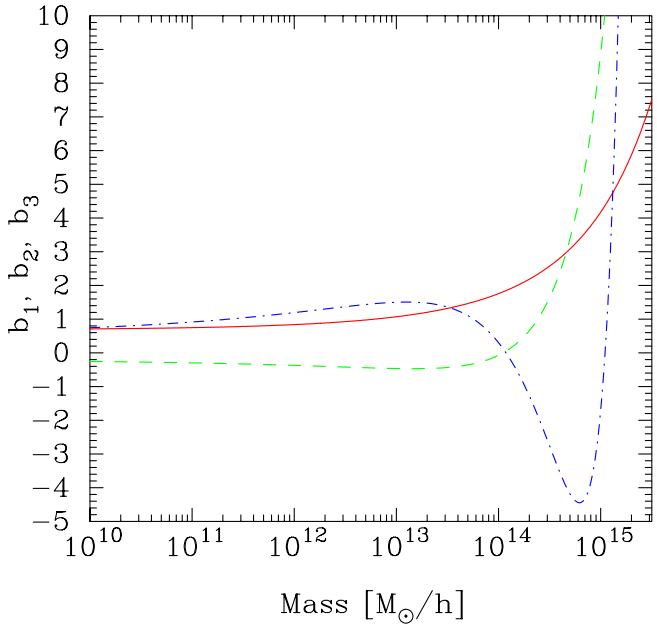

FIG. 4 (color online). First three halo bias parameters derived from the Sheth-Tormen [14] mass function as a function of halo mass [15]. The solid line shows b_1, the dashed line b_2, and the dot-dashed line b_3.

particular order. However, since the procedure that we have adopted for doing this requires some further knowledge, we shall reserve our discussion until Sec. V B.

D. Halo PT: Evolution of halo fields

We now evolve the halo density field as expressed by Eq. (30) into the nonlinear regime via perturbation theory techniques. For a short discussion of these methods see Appendix C, and for a full and detailed review see [10]. The main idea that we require from perturbation theory is that each Fourier mode of the density field may be expanded as a series,

$$\delta(\mathbf{k}, a) = \sum_i D_1^i(a)\delta_i(\mathbf{k}), \tag{35}$$

where $\delta_i(\mathbf{k})$ is the ith order Eulerian perturbation and $D_1(a)$ is the linear growth factor. Thus, on Fourier transforming the halo bias relation of Eq. (30), truncated at third order, and on inserting the PT expansion from above, we arrive at (keeping up to cubic terms)

$$\begin{aligned}\delta^{\rm h}(\mathbf{k}|M, R) = {} & b_1(M)[\delta_1(\mathbf{k}|R) + \delta_2(\mathbf{k}|R) + \delta_3(\mathbf{k}|R)] \\ & + \frac{b_2(M)}{2!}\int\frac{d^3q_1}{(2\pi)^3}[\delta_1(\mathbf{q}_1|R)\delta_1(\mathbf{k}-\mathbf{q}_1|R) \\ & + 2\delta_1(\mathbf{q}|R)\delta_2(\mathbf{k}-\mathbf{q}_1|R)] \\ & + \frac{b_3(M)}{3!}\int\frac{d^3q_1 d^3q_2}{(2\pi)^6} \\ & \times \delta_1(\mathbf{q}_1|R)\delta_1(\mathbf{q}_2|R)\delta_1(\mathbf{k}-\mathbf{q}_1-\mathbf{q}_2|R),\end{aligned} \tag{36}$$

where $\delta_i(\mathbf{q}|R) \equiv W(|\mathbf{q}|R)\delta_i(\mathbf{q})$. We next insert the solutions for each order of perturbation, which are presented in Eq. (C4) of the Appendix, into Eq. (36). On rearranging terms and collecting powers of δ, the mildly nonlinear density field of dark matter haloes may be written as a PT series expansion of the dark matter density. This series is

$$\delta^{\rm h}(\mathbf{k}, a|M, R) = \sum_{n=1}^{\infty} D_1^n(a)[\delta^{\rm h}(\mathbf{k}|M)]_n; \tag{37}$$

$$\begin{aligned}[\delta^{\rm h}(\mathbf{k}|M, R)]_n = {} & \int\frac{\prod_{i=1}^n\{d^3q_i\delta_1(\mathbf{q}_i)\}}{(2\pi)^{3n-3}} \\ & \times[\delta^D(\mathbf{k})]_n F_n^{\rm h}(\mathbf{q}_1, \ldots, \mathbf{q}_n|M, R),\end{aligned} \tag{38}$$

where $[\delta^{\rm h}(\mathbf{k}|M)]_n$ is the nth order perturbation to the halo density field, and where the short-hand notation $[\delta^D(\mathbf{k})]_n = \delta^D(\mathbf{k}-\mathbf{q}_1-\cdots-\mathbf{q}_n)$ has been used. The functions $F_n^{\rm h}(\mathbf{q}_1, \ldots, \mathbf{q}_n|M, R)$ are the halo-PT kernels, symmetrized in all of their arguments. The first three may be written in terms of the dark matter PT kernels:

$$F_1^{\rm h} = b_1(M)W(|\mathbf{k}|R)F_1; \tag{39}$$

$$\begin{aligned}F_{1,2}^{\rm h} = {} & b_1(M)W(|\mathbf{k}|R)F_{1,2} \\ & + \frac{b_2(M)}{2}W(|\mathbf{q}_1|R)W(|\mathbf{q}_2|R)F_1F_2;\end{aligned} \tag{40}$$

$$\begin{aligned}F_{1,2,3}^{\rm h} = {} & b_1(M)W(|\mathbf{k}|R)F_{1,2,3} + \frac{b_2(M)}{3}[W(|\mathbf{q}_1+\mathbf{q}_2|R) \\ & + W(|\mathbf{q}_3|R)F_{1,2}F_3 + 2{\rm cyc}] \\ & + \frac{b_3(M)}{6}W(|\mathbf{q}_1|R)W(|\mathbf{q}_2|R)W(|\mathbf{q}_3|R)F_1F_2F_3,\end{aligned} \tag{41}$$

where $F_{1,\ldots,j}^{\rm h} \equiv F_j^{\rm h}(\mathbf{q}_1, \ldots, \mathbf{q}_j|M, R)$. Thus Eqs. (37) and (38) can be used to describe the mildly nonlinear evolution of dark matter halo density fields to arbitrary order in the dark matter perturbation, and Eqs. (39)–(41) make explicit the halo evolution up to 3rd order. Together, these ideas define our meaning of the term halo-PT.

It is now apparent that halo clustering studies which assume a linear bias model and take the power spectrum to be the fully nonlinear one, are effectively assuming that $\delta^{\rm h}(\mathbf{k}|M) = b_1(M)\sum\delta_i(\mathbf{k})$, with $b_i(M) \ll b_1(M)$ for $i \neq 1$. However, for CDM, the peak-background split argument informs us that this never happens, unless the density field itself is linear [11–15]. *We must therefore conclude that extrapolating the linear bias relation into the weakly nonlinear regime, without full consideration of the nonlinearity of halo bias is incorrect.*

V. THE 1-LOOP HALO MODEL

A. Halo center power spectra

We now use the halo-PT to calculate the power spectrum of halo centers in the mildly nonlinear regime. We define the power spectrum of halo centers for haloes with masses M_1 and M_2 to be

$$\langle\delta_{\rm c}^{\rm h}(\mathbf{k}_1|M_1)\delta_{\rm c}^{\rm h}(\mathbf{k}_2|M_2)\rangle = (2\pi)^3\delta^D(\mathbf{k}_{12})P_{\rm c}^{\rm hh}(\mathbf{k}_1|M_1, M_2). \tag{42}$$

On inserting the halo-PT solutions for each order of the perturbation we find that $P_{\rm c}^{\rm hh}(k)$ can be written as the sum of three terms

$$\begin{aligned}P_{\rm c}^{\rm hh}(k|M_1, M_2) = {} & P_{\rm c,11}^{\rm hh}(k|M_1, M_2) + P_{\rm c,22}^{\rm hh}(k|M_1, M_2) \\ & + 2P_{\rm c,13}^{\rm hh}(k|M_1, M_2),\end{aligned} \tag{43}$$

where

$$P_{\rm c,11}^{\rm hh}(k|M_1, M_2) = F_1^{\rm h}(k|M_1)F_1^{\rm h}(k|M_2)P_{11}(k); \tag{44}$$

$$\begin{aligned}P_{\rm c,22}^{\rm hh}(k|M_1, M_2) = {} & 2\int\frac{d^3q}{(2\pi)^3}P_{11}(q)P_{11}(|\mathbf{k}-\mathbf{q}|) \\ & \times F_2^{\rm h}(\mathbf{q}, \mathbf{k}-\mathbf{q}|M_1)F_2^{\rm h}(\mathbf{q}, \mathbf{k}-\mathbf{q}|M_2);\end{aligned} \tag{45}$$

$$P^{\rm hh}_{\rm c,13}(k|M_1,M_2) = 6P_{11}(k)\int\frac{d^3q}{(2\pi)^3} \times P_{11}(q)\bar{F}^{\rm hh}_{13}(\mathbf{k},\mathbf{q}|M_1,M_2). \quad (46)$$

Here $P_{11}(k)$ is equivalent to the linear theory power spectrum and

$$\bar{F}^{\rm hh}_{13}(\mathbf{k},\mathbf{q}|M_1,M_2) = \tfrac{1}{2}[F^{\rm h}_1(\mathbf{k}|M_1)F^{\rm h}_3(\mathbf{k},\mathbf{q}_1,-\mathbf{q}_1|M_2) + F^{\rm h}_1(\mathbf{k}|M_2)F^{\rm h}_3(\mathbf{k},\mathbf{q}_1,-\mathbf{q}_1|M_1)]. \quad (47)$$

When these expressions are averaged over all halo masses, weighted by the respective cosmic abundances $M_1n(M_1)$ and $M_2n(M_2)$, then the constraint equation (34) guarantees that they reduce to the standard 1-loop expression for the PT power spectrum of dark matter [10]:

$$P_{\text{1-Loop}}(k) = P_{11}(k) + P_{22}(k) + P_{13}(k). \quad (48)$$

Strictly speaking the 1-loop power spectrum refers to $P_{22} + P_{13}$, we shall break convention and use Eq. (48) to define what we mean. Explicit details of the 1-loop expressions may be found in Appendix C 2.

The theory may be further developed by directly substituting the halo-PT kernels, given by Eqs. (39)–(41), into Eqs. (44)–(46). A little algebra shows that

$$\frac{P^{\rm hh}_{\rm c}(k|M_1,M_2,R)}{|W(kR)|^2} = b_1(M_1)b_1(M_2)P_{\text{1-Loop}}(k) + \bar{b}_{1,3}(M_1,M_2)\sigma^2(R)P_{11}(k) + 2\bar{b}_{1,2}(M_1,M_2)\int\frac{d^3q}{(2\pi)^3}\frac{W(qR)W(|\mathbf{k}-\mathbf{q}|R)}{W(kR)}P_{11}(q)\{P_{11}(|\mathbf{k}-\mathbf{q}|)F_2(\mathbf{q},\mathbf{k}-\mathbf{q}) + 2P_{11}(k)F_2(\mathbf{k},-\mathbf{q})\} + \frac{b_2(M_1)b_2(M_2)}{2}\int\frac{d^3q}{(2\pi)^3}\frac{|W(qR)|^2|W(|\mathbf{k}-\mathbf{q}|R)|^2}{|W(kR)|^2}P_{11}(\mathbf{q})P_{11}(|\mathbf{k}-\mathbf{q}|), \quad (49)$$

where

$$\bar{b}_{i,j}(M_1,M_2) \equiv \tfrac{1}{2}[b_i(M_1)b_j(M_2) + b_j(M_1)b_i(M_2)]. \quad (50)$$

Before continuing, we point out and answer an important question that naturally arises at this junction: How does one compare the filtered theory with the unfiltered observations? We forward the proposition that the unfiltered nonlinear power spectrum can be recovered through the following simple operation:

$$P(k|R)/|W(kR)|^2 = P(k). \quad (51)$$

This is unquestionably true for an observed nonlinear field. It will therefore also be true for the *correct* theoretical model.

This rather lengthy expression may be more readily digested through the examination of two limiting cases. But first, notice the important fact that it is still a separable product of mass dependent terms and scale-dependent terms.

When the two halo masses are identical, then

$$\frac{P^{\rm hh}_{\rm c}(k|M_1=M_2,R)}{|W(kR)|^2} = b_1^2(M)P_{\text{1-Loop}}(k) + b_1(M)b_3(M)\sigma^2(R)P_{11}(k) + b_1(M)b_2(M)\int\frac{d^3q}{(2\pi)^3}\frac{W(qR)W(|\mathbf{k}-\mathbf{q}|R)}{W(kR)}P_{11}(q) \times\left\{2P_{11}(|\mathbf{k}-\mathbf{q}|)F_2(\mathbf{q},\mathbf{k}-\mathbf{q}) + 4P_{11}(k)F_2(\mathbf{k},-\mathbf{q})\right\} + \frac{b_2^2(M)}{2}\int\frac{d^3q}{(2\pi)^3}\frac{|W(qR)|^2|W(|\mathbf{k}-\mathbf{q}|R)|^2}{|W(kR)|^2}P_{11}(q)P_{11}(|\mathbf{k}-\mathbf{q}|). \quad (52)$$

This expression is equivalent to evolving the nonlinear, local, galaxy bias model [16] through Eulerian PT. This has been explored by [73,74].

Second, consider the case where we integrate over one of the halo masses, say M_2, weighting by M_2 and its abundance $n(M_2)$. Equation (34) again insures that all terms involving $b_2(M_2)$ and $b_3(M_2)$ vanish, and so the resulting expression is the 1-loop correction to the halo center-dark matter cross-power spectrum:

$$\frac{P^{\delta\rm h}_{\rm c}(k|M,R)}{|W(kR)|^2} = \left\{b_1(M)P_{\text{1Loop}}(k) + \frac{1}{2}b_3(M)\sigma^2(R)P_{11}(k)\right\} + b_2(M)\int\frac{d^3q}{(2\pi)^3}\frac{W(qR)W(|\mathbf{k}-\mathbf{q}|R)}{W(kR)} \times P_{11}(q)[P_{11}(|\mathbf{k}-\mathbf{q}|)F_2(\mathbf{q},\mathbf{k}-\mathbf{q}) + 2P_{11}(k)F_2(\mathbf{k},-\mathbf{q})]. \quad (53)$$

Inspection of these two limiting cases reveals three remarkable features:

(i) First, if the nonlinear bias parameters $b_2(M)$ and $b_3(M)$ are nonvanishing then the bias on large scales is not $b_1(M)$.

(ii) Second, the halo-halo spectrum has a term that corresponds to constant power on very large scales, whereas the cross spectrum does not.

Both of these points were independently noted by [73,74], but for the case of nonlinear galaxy biasing (also see [35]).

(i) Third, the large-scale bias derived from the halo-dark matter cross-power spectrum is not b_1, nor is it given by the bias derived from the halo-halo power spectrum.

To see these points more clearly we take the $k \to 0$ limit of Eqs. (49), (52), and (53):

$$P_c^{hh}(k|M_1, M_2, R) = b_1(M_1)b_1(M_2)P_{11}(k)\Big\{1 + \sigma^2(R)\Big[\frac{34}{21} \times \Big(\frac{b_2(M_1)}{b_1(M_1)} + \frac{b_2(M_2)}{b_1(M_2)}\Big) + \frac{1}{2}\Big(\frac{b_3(M_1)}{b_1(M_1)} + \frac{b_3(M_2)}{b_1(M_2)}\Big)\Big]\Big\} + \frac{b_2(M_1)b_2(M_2)}{2} \times \int \frac{d^3q}{(2\pi)^3}[P_{11}(q)|W(qR)|^2]^2; \quad (54)$$

$$P_c^{hh}(k|M, R) = b_1^2(M)P_{11}(k)\Big\{1 + \sigma^2(R)\Big[\frac{68}{21}\frac{b_2(M)}{b_1(M)} + \frac{b_3(M)}{b_1(M)}\Big]\Big\} + \frac{b_2^2(M)}{2}\int \frac{d^3q}{(2\pi)^3} \times [P_{11}(q)|W(qR)|^2]^2; \quad (55)$$

$$P_c^{\delta h}(k|M, R) = b_1(M)P_{11}(k)\Big\{1 + \sigma^2(R)\Big[\frac{34}{21}\frac{b_2(M)}{b_1(M)} + \frac{1}{2}\frac{b_3(M)}{b_1(M)}\Big]\Big\}. \quad (56)$$

These expressions make the first point noted above trivially obvious: The large-scale bias is modulated by the halo-PT correction terms, and these depend on the nonlinear bias parameters b_2 and b_3 and also on the filtered variance of fluctuations.

The second point noted above originates specifically from the quadratic nonlinear bias terms found in Eqs. (54) and (55), e.g. terms containing $b_2(M_1)b_2(M_2)$ and $b_2^2(M)$. For a linear power spectrum that obeys the limit $P_{11}(k \to 0) \to 0$, these expressions reduce to the constant

$$P_c^{hh}(k \to 0|M) = \frac{b_2^2(M)}{2}\int \frac{d^3q}{(2\pi)^3}[P_{11}(q)|W(qR)|^2]^2. \quad (57)$$

This term was discussed in great detail for the case of galaxy biasing by [73].

The third point noted above can be understood by constructing the linear bias, e.g. dividing Eqs. (55) and (56) by P_{11}. On squaring the bias recovered from (56) and subtracting it from the bias from (55), we find

$$\{[b_{Lin}^{hh}]^2 - [b_{Lin}^{\delta h}]^2\} = \frac{b_2^2(M)}{2P_{11}(k)}\int \frac{d^3q}{(2\pi)^3}[P_{11}(q)|W(qR)|^2]^2 - \sigma^4(R)\Big\{\frac{34}{21}b_2(M) + \frac{1}{2}b_3(M)\Big\}^2, \quad (58)$$

We now see that, because P^{hh} approaches a constant on very large scales, on dividing through by $P_{11}(k|M)$ the bias function b^{hh} diverges at the origin as $1/P_{11}^{1/2}$ diverges.

Figure 5 shows our expressions for b_{Lin}^{hh} and $b_{Lin}^{\delta h}$ (from Eqs. (54) and (55)). In this particular case, we assume the nonlinear bias parameters derived from the Sheth-Tormen mass function by [15]. We use a Gaussian filter, for which $W(kR_G) = \exp[-(kR)^2/2]$. For $R_G = 20h^{-1}$ Mpc and for our fiducial cosmology, we find $\sigma^2(R_G = 20) \approx 0.046$. To inspect the differences more closely, we take the ratio of the predictions with respect to the tree-level theory, e.g. $b_1 = P_{11}^{\delta h}/P_{11} = \sqrt{P_{11}^{hh}/P_{11}}$. The figure demonstrates two of the points raised above. First the large-scale bias is not simply b_1: halo-halo bias (solid through to dotted curves) does not converge as one considers larger and larger scales; however bias from the cross-power spectrum is very close to linear for all except the most massive haloes, where b_2

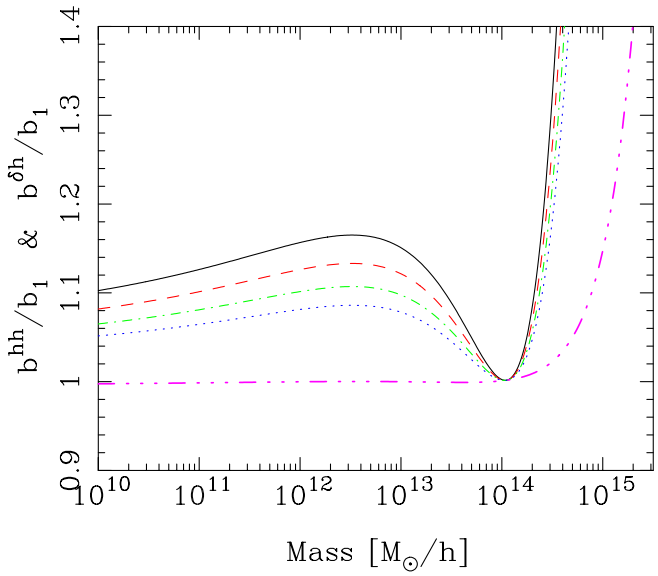

FIG. 5 (color online). 1-loop bias parameters b^{hh} and $b^{\delta h}$ in the ultra large-scale limit. The solid through to dotted curves show b^{hh}, measured on scales ($k_{obs} = \{0.001, 0.005, 0.01, 0.05\}h$ Mpc^{-1}), derived from the 1-loop halo-halo cross-power spectrum as a function of halo mass. The triple dot-dashed curve shows $b^{\delta h}$ as derived from the 1-loop halo-dark matter cross-power spectrum.

and b_3 are very strongly rising functions (see Fig. 4). Second, it is now obvious that $b^{\rm hh}$ and $b^{\delta{\rm h}}$ are not the same. Note also that the magnitude of the expected scale dependence: the bias varies by at most 5% when k is]changed by an order of magnitude. The mass dependence of $b^{\rm hh}$ shown in Fig. 5 is simply driven by that of $b_2^2(M)$ (again see Fig. 4). As halo mass increases the bias slowly increases until it reaches a maximum at $M \sim 10^{13}h^{-1}M_\odot$. It then decreases to $M \sim 10^{14}h^{-1}M_\odot$ after which it shoots up dramatically for larger masses.

B. Convergence of the power spectrum

We now return to the issue of truncation and applicability of the Taylor series expansion of the halo field. A first requirement for the Taylor series to converge after a finite number of terms is that the filter scale be large enough so that the r.m.s. dark matter fluctuations be much less than unity: $\sigma(R) \ll 1$. Considering the case where R is very large and convergence occurs at first order, we then have: $\delta^{\rm h}(\mathbf{x}|R) = b_1(M)\delta_1(\mathbf{x}|R)$. As the filter scale R is slowly decreased the r.m.s. fluctuations in δ increase and a larger and larger number of terms are required to accurately map the underlying bias function. Finally, as $\sigma(R) \to 1$ all terms in the series are required. At this point the method has no merit.

Since a robust criterion for truncation is out of reach at the present, we propose an *ad hoc* criterion for convergence that must plausibly be obeyed, that is

$$b_1(M)\sigma(R) < 1. \tag{59}$$

In Appendix B we shall also discuss an empirical method for testing convergence.

C. Returning to the halo model

We now translate these ideas back into the language of the halo model. To begin, we shall restrict our attention to the halo model in the large-scale limit, more precisely we consider scales where $U(k|M) \sim 1$. Since the Fourier transform of the mass normalized profile may be written

$$U(k|M) = \int_0^{r_{\rm vir}} d^3r U(r|M)\frac{\sin[kr]}{kr}, \tag{60}$$

our large-scale condition simply becomes $kr_{\rm vir} \ll 1$. In the above equation we have, for convenience, assumed spherical density profiles. If halo mass and virial radius are related through $M = 4\pi 200\bar{\rho}r_{\rm vir}^3/3$, then for the largest collapsed objects in the Universe $M \approx 10^{15}h^{-1}M_\odot$, and the above condition translates to the inequality $k \ll 0.4h$ Mpc^{-1}. If we assume an NFW density profile [75] with concentration parameter $c \sim 6$, then for $k \sim 0.15h$ Mpc^{-1}, we find that $U(k) \approx 0.994$. We therefore assume that this is an excellent approximation over the scales that we are interested in.

Hence for scales $kr_{\rm vir} \ll 1$, our Eqs. (22) and (23), at the 1-loop level in halo-PT, now take the forms:

$$\frac{P_{\rm 1H}^{ij}(\mathbf{k}|R)}{|W(kR)|^2} = \frac{1}{\bar{\rho}^i\bar{\rho}^j}\int_0^\infty dMn(M)M^2\Theta_{ij}(M, M); \tag{61}$$

$$\frac{P_{\rm 2H}^{ij}(\mathbf{k}|R)}{|W(kR)|^2} = \frac{1}{\bar{\rho}^i\bar{\rho}^j}\int_0^\infty \prod_{l=1}^{2}\{dM_l n(M_l)M_l\} \times \frac{P_{\rm c}^{\rm hh}(\mathbf{k}|M_1, M_2, R)}{|W(kR)|^2}\Theta_{ij}(M_1, M_2), \tag{62}$$

where we have explicitly included a filter on the 1-halo term. (Recall that the halo center power spectrum in the 2-halo term already includes such a filter.)

We now see that, because the $b_i(M)$ are the only mass dependent functions, on insertion of Eq. (49) into Eq. (62) the integrals over mass may be immediately computed. Thus,

$$P_{\rm 2H}^{ij}(\mathbf{k}|R) = P^{ij,{\rm hh}}(\mathbf{k}|R), \tag{63}$$

where $P^{ij,{\rm hh}}(\mathbf{k}|R)$ is equivalent to Eq. (49), except that we have replaced all of the mass dependent bias parameters by the average ones: i.e.

$$\langle b_i\rangle \equiv \frac{\int_0^\infty dMn(M)Mb_i(M)\Theta(M - M_{\rm cut})}{\int_0^\infty dMn(M)M\Theta(M - M_{\rm cut})}. \tag{64}$$

We note that if we wish to weight by halo number density rather than mass density then we simply remove the mass weighting in the numerator and denominator of $\langle b_i\rangle$.

VI. EVALUATION OF THE THEORY

In this section we present the results from the direct computation of the 1-loop halo center expressions for $P_{\rm c}^{\rm hh}$ and $P_{\rm c}^{\delta{\rm h}}$, as given by Eqs. (52) and (53), respectively. This section is almost entirely pedagogical; we urge those who are only interested in the direct comparison with the numerical work to press on to Sec. VII.

Recall that it is necessary to adopt some filter scale R. We have studied two choices: $R_{\rm G} = 20h^{-1}$ Mpc and $R_{\rm G} = 10h^{-1}$ Mpc for which the linear theory, Gaussian filtered, variances are $\sigma^2(R) = 0.046$ and 0.177, respectively. The larger smoothing scale is required for the more massive haloes.

A. Halo-dark matter cross-power spectra

In Fig. 6 we show the predictions for the scale dependence of $P^{\delta{\rm h}}$ at the 1-loop level, as a function of wave number. The different panels show results for different halo masses and smoothing scales. In all four panels, we see that, as expected, there is a small (few percent) positive offset from the linear theory bias value b_1. The largest offset occurs for the cluster mass haloes, but here it may be the case that, owing to the bias being large, the filter scale that we have adopted for these objects may still be too

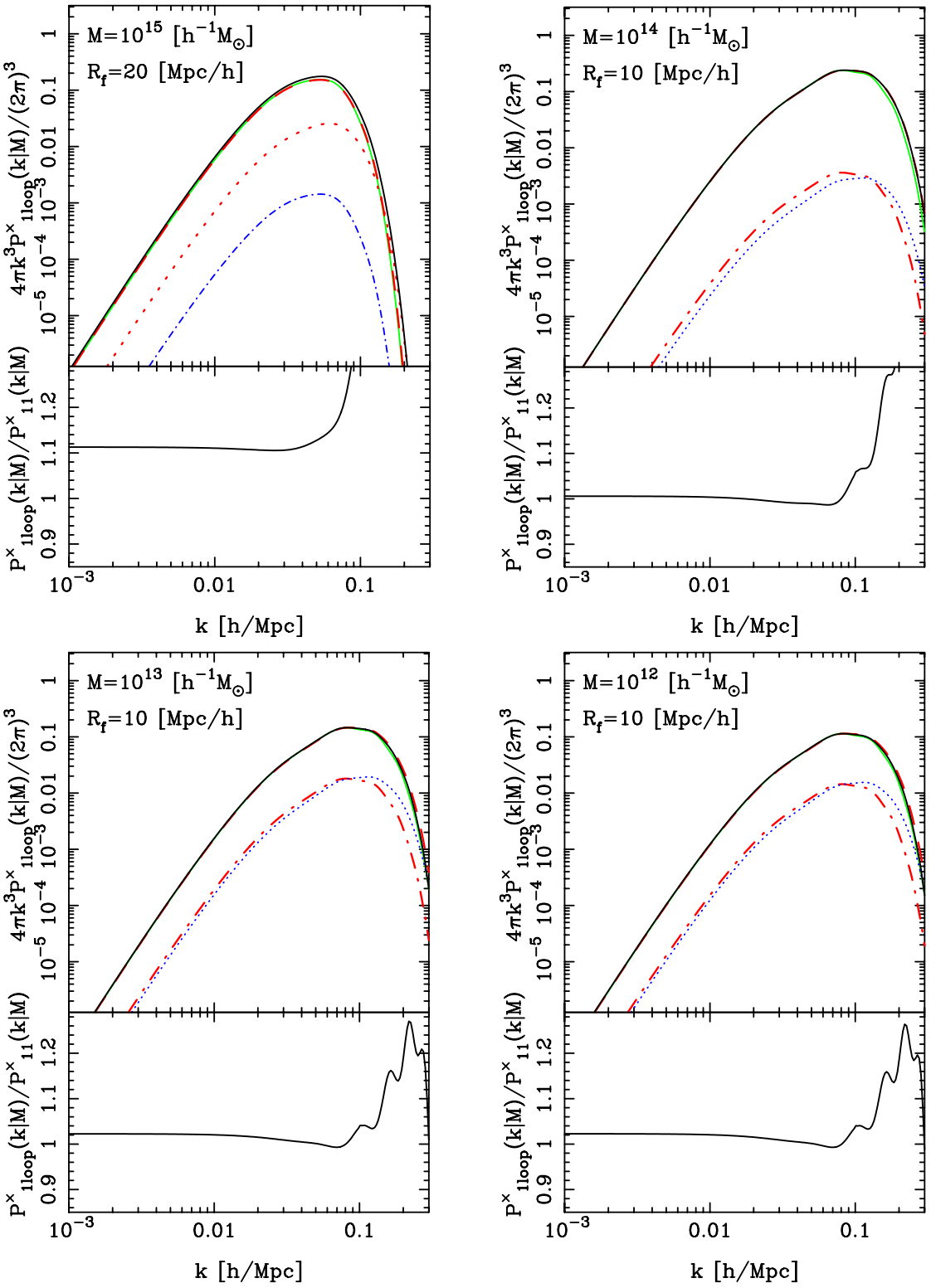

FIG. 6 (color online). The real-space cross-power spectrum of haloes and cold dark matter at the 1-loop level on large scales. The four panels show predictions for haloes with masses: $M = \{10^{15}, 10^{14}, 10^{13}, 10^{12}\}h^{-1}M_{\odot}$. In the upper plot of each panel, the thick curve represents the total spectrum as given by Eq. (53). The dashed curve gives the 1-loop contribution from the linear bias parameter b_1 term; the dotted curve and dot-dashed curves give the 1-loop contributions from the nonlinear bias parameters b_2 and b_3, and the thickness of the lines indicates their sign, with thick lines being positive and thin lines being negative contributions. The thin solid line gives the smoothed, linearly biased, linear power spectrum. The lower plot of each panel shows the ratio of the total cross spectrum with the smoothed linear theory cross spectrum.

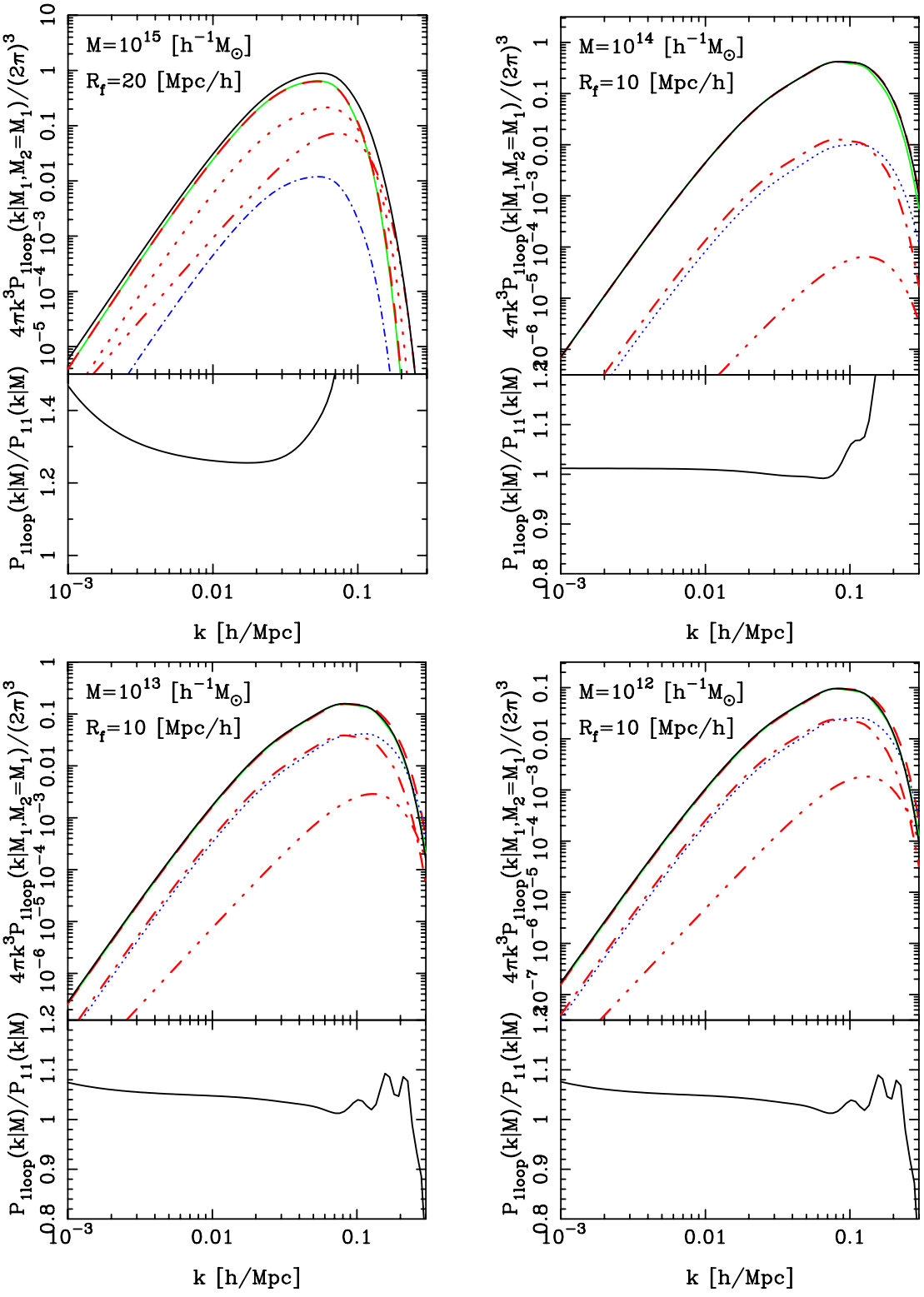

FIG. 7 (color online). The real-space halo-halo power spectrum at the 1-loop level on large scales. The four panels show predictions for haloes with masses: $M = \{10^{15}, 10^{14}, 10^{13}, 10^{12}\}h^{-1}M_\odot$. In the upper panels of each subfigure, the thick curve represents the total spectrum as given by Eq. (52), the dashed curve represents the 1-loop contribution from the pure linear bias (b_1^2) term, the dotted and dot-dashed curves represent the 1-loop contributions from the $b_2 b_1$ and $b_3 b_1$ terms, respectively. The triple dot-dashed curve represents the quadratic nonlinear bias term b_2^2. Lastly, the thin solid line denotes the smoothed, linearly biased linear theory spectrum. As before, line thickness distinguishes positive and negative contributions. Bottom panels show the ratio with the linear spectrum.

small for adequate convergence. We also note that the offset for the $M = 10^{14}h^{-1}M_\odot$ haloes is negligible. This can be attributed to the fact that $b_2 \approx b_3 \approx 0$ (see Fig. 4). For the lower mass haloes the offsets are roughly $\sim 2\%$ in excess of linear.

Considering the predictions for the highest mass haloes, we see that the spectrum is scale independent up to $k \sim 0.07h$ Mpc^{-1}, where the nonlinear amplification from the P_{22} term becomes dominant. For this case, the absence of the previrialization feature may be understood as follows: First, we note that b_1 and b_2 are positive, whereas b_3 is negative. However, since b_3 is an order of magnitude smaller than the others, it plays no significant part in determining the shape of the spectrum. The P_{13} term in the 1-loop power spectrum, which is the main cause of the previrialization feature, is thus overwhelmed by the action of the quadratic bias b_2 term. This suggests that $P^{\delta h}$ should be scale independent up to $k \sim 0.07h$ Mpc^{-1}.

Next, we collectively consider the predictions for the lower mass haloes, as they show many similar traits. First, we find that when $k < 0.01h$ Mpc^{-1}, then the ratios of the 1-loop to tree-level (or linear) spectra are flat. However, for $0.01h$ Mpc$^{-1} < k < 0.07h$ Mpc^{-1}, significant scale dependence is apparent: the previrialization feature is present and it appears to become stronger as halo mass decreases. On smaller scales still, the nonlinear boost from the P_{22} term amplifies the power spectrum and breaks all scale independence. Interestingly, the onset of P_{22} is pushed to smaller scales as halo mass decreases. These effects can be understood as follows. For these objects b_1 and b_3 are positive, whereas b_2 is negative. On large scales, we see that b_2 and b_3 are nearly equivalent, but b_3 is slightly dominant, and this results in a small positive correction. Whereas on smaller scales this trend reverses and b_2 becomes dominant. The overall correction is then negative and this leads to the enhanced previrialization feature and delay of the onset of P_{22}.

It is also interesting to note the imprint of the BAO features in the ratios of the power spectra. The strength of the signal appears to depend on halo mass and increases as halo mass decreases. As we discussed in Sec. III C, this can be attributed to the fact that nonlinear evolution suppresses BAOs on small scales, and on taking the ratio with a linear theory spectrum, we are artificially introducing oscillations.

B. Halo-halo power spectra

In Fig. 7 we show the predictions for the scale dependence of $P^{\rm hh}$, at the 1-loop level, as a function of wave number. The four panels show results for haloes with masses in the same range as Fig. 6. Again, upper panels show the contributions from each of the halo-PT terms in Eq. (52), and where the sign of each contribution is distinguished through line thickness/color. Subpanels are as before.

Some obvious similarities exist between the autohalo spectra and the cross spectra. In particular: the large-scale bias is not given by b_1; the highest mass halo spectrum shows no sign of the previrialization power decrement; the nonlinear boost occurs increasingly at smaller scales as halo mass decreases; with the exception of the highest mass haloes, the ratio of the 1-loop spectra to the tree-level spectra have BAOs imprinted. These effects may all be understood through the explanations from the previous subsection.

We also notice some important differences between $P^{\rm hh}$ and $P^{\delta h}$. First, the addition of the quadratic nonlinear bias term, $[b_2(M)]^2$, modifies the results on the largest scales. As was discussed in Sec. V, $P^{\rm hh}_{\rm 1\text{-}Loop}$ becomes a white-noise power spectrum as $P_{11} \to 0$, unless $b_2 = 0$. In the figure, the contributions from this term are denoted by the triple dot-dashed lines. On considering all four panels and paying special attention to the ratios, we see that, with the exception of the case $M \sim 10^{14}h^{-1}M_\odot$, there is an upturn in power on scales $k < 0.01h$ Mpc^{-1}. For the $M \sim 10^{14}h^{-1}M_\odot$ haloes this effect is not found, this owes to the fact that $b_2 \sim 0$ (see Fig. 4).

Second, we note that on smaller scales the effect of the b_2^2 term is to boost the power across all scales. Thus the previrialization power decrement is no longer a decrement relative to the linear theory. However, relative to the power measured on say $k \sim 0.01h$ Mpc^{-1}, there is a very real decrement. Moreover, the k-dependence of the terms multiplying b_2^2 will make the decrement appear larger than we would expect from the nonlinear matter spectrum.

C. Nonlinear evolution of BAOs

We now briefly consider how mode-mode coupling and nonlinear biasing affect the evolution of the BAOs. Figure 8 compares the 1-loop predictions for $P^{\rm hh}$ with the linear theory predictions. We again consider the set of halo masses: $M = \{10^{15}, 10^{14}, 10^{13}, 10^{12}\}h^{-1}M_\odot$, and, to emphasize the evolution of the BAO features, we have taken the ratio of each spectrum with the No-Baryon model of Eq. (12). In addition, because we are purely interested in the scale dependence, we renormalize all ratios to unity at $k \sim 0.01h$ Mpc^{-1}.

The top-left panel shows results for the highest mass haloes: all but the first of the BAO troughs has been removed through nonlinear evolution. This is a much more aggressive nonlinear evolution than one expects from considerations of the dark matter alone. Second, the trough appears to have been displaced towards lower frequencies. These effects arise because both the quadratic bias (b_2^2) and $b_2 b_1$ terms are positive, and so dominate over the negative b_3 and P^{13} terms. This fact, coupled with the injection of power from P_{22}, means that the nonlinear boost occurs at $k \sim 0.05h$ Mpc^{-1}. Thus, the overall effect on the halo spectrum is to shift the first trough to smaller k.

All the spectra of the lower mass haloes display a previrialization feature, the strength of which increases as

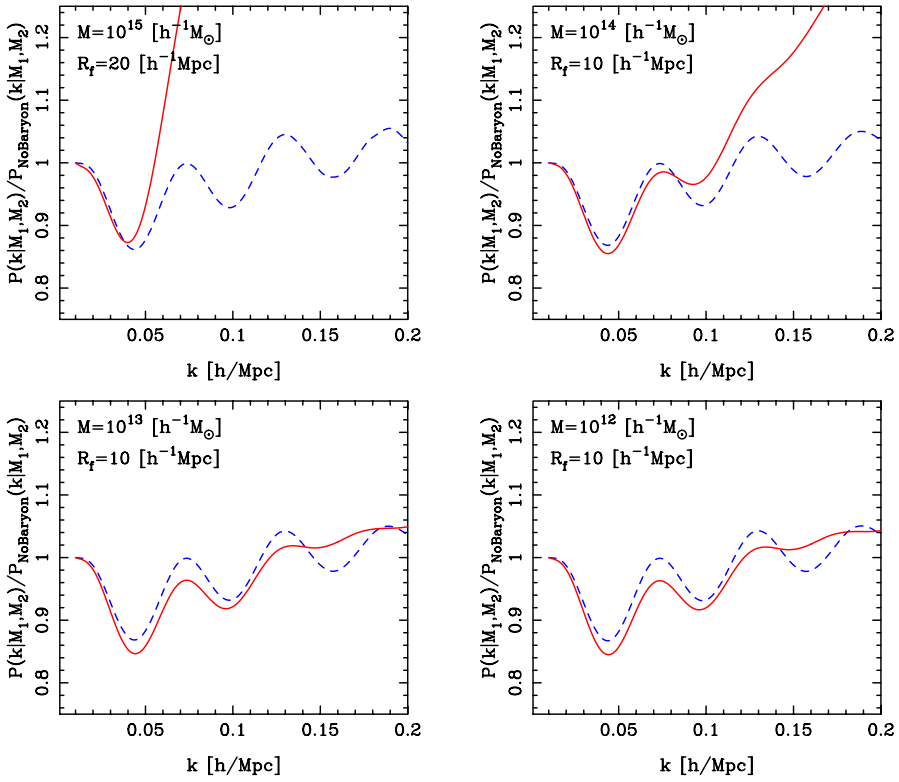

FIG. 8 (color online). Nonlinear evolution of the BAOs as traced by the halo-halo power spectrum for four different halo masses. The solid line denotes the nonlinear (1-loop) spectrum as given by Eq. ; the dashed line denotes the linear theory (tree-level) power spectrum. We have taken the ratio of each spectrum with a smooth No-Baryon model as described in the text, and have renormalized each spectrum so that they are unity on a scale $k \sim 0.01h$ Mpc^{-1}.

halo mass decreases. In addition, the number of peaks and troughs which remain in the evolved spectra increases as halo mass decreases, because the strong nonlinear amplification from the P_{22} term is delayed by the negative $b_2 b_1$ corrections. However, in contrast to the high mass haloes, for the low mass haloes the first acoustic trough is shifted towards larger k because, when $0.01 < k < 0.05$, then the negative correction from the $b_2 b_1$ term is dominant and so subtracts power from the higher frequency side of the oscillation. This acts to shift the overall pattern to higher frequencies.

VII. COMPARISON WITH SIMULATIONS

In this section, we compare the predictions from the theoretical model with the results from the numerical simulations presented in Sec. III.

A. Halo center power spectra revisited

Returning to our analysis of Fig. 1, we are now in a position to comment on the success of the halo-PT model in comparison to the numerical simulations. The analytic model was evaluated using the semiempirical bias parameters that were determined as described in Appendix B. Since here we are concerned purely with the scale dependence of the spectra and not their overall amplitude, we allowed the very large-scale normalizations to be considered as free parameters. These were fit for in exactly the same way as was done for the linear theory models in Eq. (13). Whilst this rescaling would not be necessary if the bias parameters that we were adopting were precise and accurate, since we have not been able to establish this in a robust manner we feel that this approach is acceptable, given that it has been equally applied to the linear theory. Moreover, this is the method of analyzing real data.

These predictions are shown as the solid lines in Fig. 1. Comparison with the measured $P_{\rm c}^{\rm hh}$, shows that the model and the shot-noise corrected data show reasonable correspondence over scales $k < 0.07h^{-1}$ Mpc. On smaller scales the match is poor. However, the uncertainty in the shot-noise correction makes it very difficult to draw firm conclusions.

Considering $P^{\delta{\rm h}}$, we find that the analytic model is in good agreement with the simulations over a much larger range of scales. The model correctly captures the mass dependence of the previrialization feature—low mass haloes show greater loss of memory to the initial density fluctuations. The shifting of the nonlinear boost to smaller scales as halo mass decreases is also matched rather well.

To assess whether $P_{\rm c,1\text{-}Loop}^{\delta{\rm h}}$ is a better fit to the simulation data than is linear theory, we have performed a likelihood ratio test, assuming that the likelihood functions are

Gaussian. In this case, a necessary statistic for model selection is for

$$\mathrm{LR} \equiv \frac{\mathcal{L}(\{x_l, y_l\}|[P^{ij}_{\text{1-Loop}}]_{\max})}{\mathcal{L}(\{x_l, y_l\}|[P^{ij}_{\text{Lin}}]_{\max})} > 1, \tag{65}$$

where the subscript "max" refers to the parameter choices in the models that maximize the likelihood. Restricting the information to be $k < 0.1h$ Mpc^{-1}, we find, going from low to high mass haloes, that LR $= \{1.06, 1.03, 1.05, 1.07\}$, respectively.

B. Halo bias revisited

We now examine how well the halo-PT model does at matching the nonlinear scale-dependent bias of the halo centers as measured in the numerical simulations (Fig. 2). The top section of each panel shows that the analytic model (solid lines correspond to $b^{\delta h}_{\text{NL}}$ and $b^{\text{hh}}_{\text{NL}}$, respectively) captures, qualitatively, the scale dependence of the bias. The model shows a bias that increases with k for the high mass haloes but decreases with k for lower masses. However, there are some notable discrepancies: The model underpredicts and then overshoots the measured relationship for the most massive haloes; for the next bin in halo mass (top-right panel), the measured bias is flat, whereas the model predicts a down turn after $k \sim 0.1h$ Mpc^{-1}; the model fares better in the two lowest mass bins, but the down turn at high k is not seen in the data. However, we must stress that, with the exception of the $M \sim 10^{14}h^{-1}M_\odot$ haloes, the model outperforms linear theory, which would predict constant bias on all scales.

Having extolled the virtues of our model we now draw attention to its shortcomings. Whilst the predictions provide a good match to the halo power spectra, they do not simultaneously provide a good match to the scale dependence of the bias. If we reconsider our measurements of the nonlinear matter power spectrum (upper sections in Fig. 1) $P^{\delta\delta}$, we see that the 1-loop model (dot-dashed lines) overpredicts the LR simulations on scales $k > 0.05h$ Mpc^{-1} and the HR simulations on scales $k > 0.07h$ Mpc^{-1}. It is therefore unlikely that the model as presented here can be made to work precisely.

VIII. GALAXY POWER SPECTRUM

How does the scale dependence of the bias depend on galaxy type? The answer has important consequences for future galaxy surveys that will measure the clustering of specific subclasses of objects. We may address this question using the halo model by changing the mass weighting in the integrals to:

$$\begin{aligned} n(M)M &\to n(M)\langle N|M\rangle; \\ n(M)M^2 &\to n(M)\langle N(N-1)|M\rangle, \end{aligned} \tag{66}$$

where $\langle N|M\rangle$ and $\langle N(N-1)|M\rangle$ are the first two factorial moments of the halo occupation probability function $P(N|M)$, which gives the probability for a halo of mass M to host N galaxies. Use of the factorial moments of $P(N|M)$ subtracts off a term corresponding to the self-correlation of galaxies, e.g. $\xi(r \to 0) = \delta^D(r)/\bar{n}$. This corresponds to the Poisson shot-noise term in Fourier space. Second, the mean density profile of dark matter is changed to the mean density profile of galaxies in the halo: $U(k|M) \to U^{\text{g}}(k|M)$. Following the discussion in Sec. V C, it is a very good approximation to set $U^{\text{g}}(k|M) = 1$ when $kr_{\text{vir}} \ll 1$. Third, the constant prefactors transform as $1/\bar{\rho}^2 \to 1/\bar{n}^2_{\text{g}}$, where

$$\bar{n}_{\text{g}} = \int dM n(M)\langle N|M\rangle\Theta(M - M_{\text{cut}}). \tag{67}$$

And finally, the galaxy bias parameters are

$$b^{\text{g}}_i = \frac{1}{\bar{n}_{\text{g}}}\int dM n(M)\langle N(M)\rangle b_i(M). \tag{68}$$

These changes in Eqs. (61) and (62) yield the 1-loop halo-model prediction for the galaxy power spectrum. Explicitly:

$$\frac{P^{\text{gg}}_{\text{1H}}(k|R)}{|W(kR)|^2} = \frac{1}{\bar{n}^2}\int dM n(M)\langle N(N-1)|M\rangle\Theta(M - M_{\text{cut}}); \tag{69}$$

$$\frac{P^{\text{gg}}_{\text{2H}}(k|R)}{|W(kR)|^2} = \frac{1}{\bar{n}^2}\int \prod_{i=1}^{2}\{dM_i n(M_i)\langle N|M_i\rangle\Theta(M_i - M_{\text{cut}})\} \times \frac{P^{\text{hh}}_{\text{c,1-Loop}}(k|M_1, M_2, R)}{|W(kR)|^2}, \tag{70}$$

where again we have explicitly included a filter function on the 1-halo term. On inserting our expression for P^{hh}_{c} from Eq. (52) into the 2-halo term, and again noticing that in the large-scale limit the mass integrals may be performed directly, we find:

$$\begin{aligned} \frac{P^{\text{gg}}_{\text{2H}}}{|W(kR)|^2} = \{[b^{\text{g}}_1]^2 P_{\text{1-Loop}}(k) + b^{\text{g}}_1 b^{\text{g}}_3\sigma^2(R)P_{11}(k)\} + \frac{[b^{\text{g}}_2]^2}{2}\int \frac{d^3q}{(2\pi)^3}P_{11}(q)P_{11}(|\mathbf{k}-\mathbf{q}|)\frac{|W(qR)|^2|W(|\mathbf{k}-\mathbf{q}|R)|^2}{|W(kR)|^2} \\ + 2b^{\text{g}}_1 b^{\text{g}}_2\int \frac{d^3q}{(2\pi)^3}P_{11}(q)\frac{W(qR)W(|\mathbf{k}-\mathbf{q}|R)}{W(kR)}\{P_{11}(|\mathbf{k}-\mathbf{q}|)F_2(\mathbf{q}, \mathbf{k}-\mathbf{q}) + 2P_{11}(k)F_2(\mathbf{k}, -\mathbf{q})\}, \end{aligned} \tag{71}$$

The resulting expression for the galaxy power spectrum is identical to that given by [73,74], with one important difference—we include the large-scale constant power originating from $P_{1H}^{gg}(k|R)$.

To study the expected differences between red and blue galaxies, we use the parametric forms for $\langle N(M)\rangle$ measured by [76] in the semianalytic models of [77]:

$$\langle N_B|M\rangle = 0.7\left(\frac{M}{M_B}\right)^{\alpha_B}; \qquad \langle N_R|M\rangle = \left(\frac{M}{M_R}\right)^{\alpha_R}. \quad (72)$$

The blue galaxy parameters are: $M_B = 4\times10^{12}h^{-1}M_\odot$; for haloes with masses in the range $10^{11} \le M/h^{-1}M_\odot \le 4.0\times10^{12}$ then $\alpha_B = 0.0$, for larger mass haloes $\alpha_B = 0.8$. The red galaxy parameters are: $M_R = 2.5\times10^{12}h^{-1}M_\odot$; for haloes with masses greater than the cutoff mass $\alpha_R = 0.9$. For the second moment of the HOD we follow the model of Kravtsov *et al.* [78], so that $\langle N(N-1)|M\rangle = \langle N|M\rangle^2 - 1$. This makes $P(N|M)$ sub-Poissonian as suggested from the observations [20,56,63] and the semianalytic models [15,19,76,79,80]; and second, this choice allows the first moment alone to fully specify the hierarchy of moments.

In practice, we use the models above but impose a lower mass cutoff of $M_{\rm min} = 10^{12}h^{-1}M_\odot$. This yields $\bar{n}_B = 4.10\times10^{-3}h^3$ Mpc^{-3}, $\bar{n}_R = 7.93\times10^{-3}h^3$ Mpc^{-3}, $\{b_1^B = 1.20, b_2^B = -0.14, b_3^B = 1.06\}$, and $\{b_1^R = 1.39, b_2^R = 0.09, b_3^R = 0.89\}$. (This estimate of b_2^B agrees with the observational determinations of similar galaxies from the PSCz survey [81].) These values are easily understood by noting how $b_i(M)$ depends on halo mass (e.g. Fig. 4), the weightings given in Eq. (72), and recalling that the halo-mass function declines exponentially at $M > 10^{13}h^{-1}M_\odot$. Notice that the red galaxy bias parameters are all positive, whereas b_2^B for the blue galaxies is negative. Therefore, while we expect to see a previrialization feature in $P_B(k)$, we do not for the red galaxies.

The left panel of Fig. 9 shows the power spectrum of blue and red galaxies evaluated using the 1-loop halo model. The top section shows the individual contributions from all the linear and nonlinear terms. Note that, for the blue galaxies the nonlinear correction terms $b_1^Bb_2^B$ (dotted lines) and $b_1^Bb_3^B$ (dot-dashed lines) are roughly the same order of magnitude as the 1-halo term (thin line). However, for the red galaxies, the 1-halo term (thin line) dominates over the nonlinear bias corrections by factors of a few. For both populations the quadratic bias terms $[b_2^g]^2$ (triple dot-dashed lines) appear to be negligible.

The middle section of the left-hand panel shows the ratios of the 1-loop P_{2H}^{gg} with the No-Baryon linear model (from Eq. (12)). Again, since we are primarily interested in the scale dependence of the bias, we renormalize all curves to be unity at $k \sim 0.01h$ Mpc^{-1}. As expected, the red galaxy power spectrum appears to trace the linear theory matter fluctuations (dashed line) very well when $k < 0.07h$ Mpc^{-1}. The nonlinear boost breaks this accordance at larger k. However, for the blue galaxies, the scale dependence is more complicated, having an increased previrialization feature and a delayed nonlinear boost. We also note that, for the red galaxies, the second and third BAOs have been almost completely suppressed, whereas only the third peak has been removed for the blue galaxies. The peaks and troughs, however, appear to be in the right places.

So far, we have neglected the contribution from the constant power 1-halo term. In the bottom section of the panel we now take this into account and show $P_{1H}^{gg} + P_{2H}^{gg}$ ratioed to the No-Baryon model. For the red galaxies, the agreement between the predictions and the linear theory that was noticed before is now broken on much larger scales, $k \sim 0.04h$ Mpc^{-1}. The trough of the first BAO has been shifted slightly to smaller k and the nonlinear boost occurs at a larger scale. Because the 1-halo term is about 5 times smaller for the blue galaxies, the modifications are not as severe. The addition of this term offsets the suppression of power caused by the negative $b_1^Bb_2^B$ term and the blue galaxies now appear to trace the linear theory on scales $k < 0.07h$ Mpc^{-1} quite well. At larger k the linear spectrum is a poor match to the predictions. We also note that the BAOs are further suppressed and the second trough has been shifted to lower frequencies.

Because $P_{1\text{-Loop}}$ does not provide a very accurate model for the true nonlinear power spectrum, we have studied the effect of exchanging $P_{1\text{-Loop}}$ for the `halofit` [43] power spectrum. The results are shown in the right-hand panel of Fig. 9. Although the predictions are qualitatively very similar, `halofit` predicts enhanced previrialization and smaller nonlinear boosts. In the middle panel, where the 1-halo term is not included, we see that the red and blue galaxies do not match the linear theory as well on large scales. In particular the blue galaxy power is suppressed on all scales except the largest. We also see that the BAOs have been better preserved. Although there are slight shifts in the positions of the second trough and third peak. However, the bottom panel shows that once the 1-halo term has been included, the red galaxy predictions are almost as before. The blue galaxies still show a reasonably strong previrialization feature, but, because of the weak nonlinear boost, they match the linear theory rather well over nearly all the scales considered.

We note that this modification is not entirely self-consistent and as such is not meant to be blindly trusted, since the nonlinear bias terms are still derived from the 1-loop halo-PT. However, we use this operation to highlight that a more advanced understanding of the nonlinear power spectrum does change the results quantitatively. This implies that a more advanced model of the scale dependence

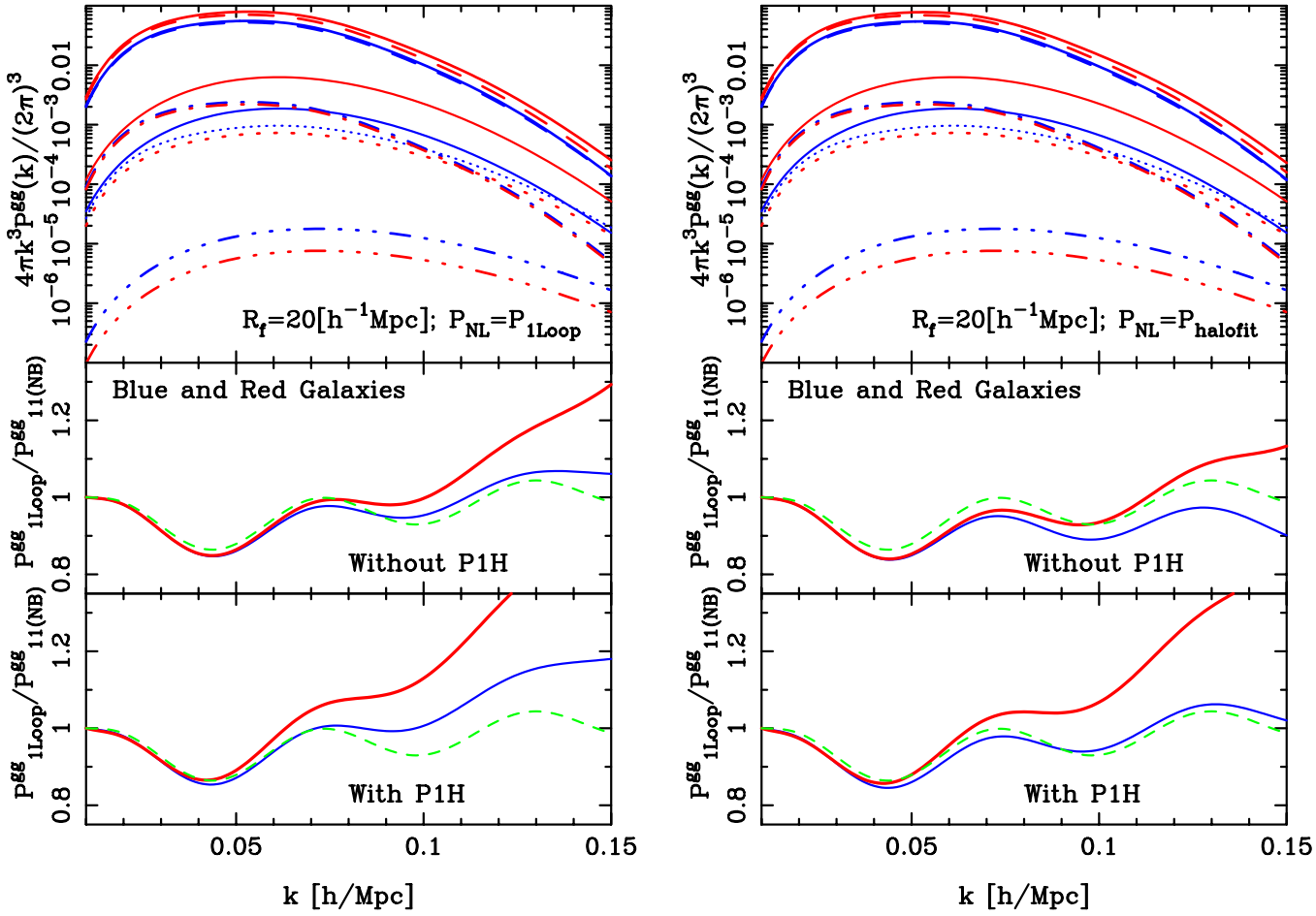

FIG. 9 (color online). Scale dependence of the power spectrum of blue and red galaxies on very large scales. Top-left panel shows the results obtained from the evaluation of Eqs. (69) and (71). The 1-halo term is represented by the thin solid lines. For the 2-halo term we have the following contributions: b_1^2 terms denoted by dashed lines; $b_2 b_1$ terms denoted by dotted lines; $b_3 b_1$ terms denoted by dot-dashed lines; b_2^2 terms denoted by triple dot-dashed lines. Note again for the 2-halo contributions, line thickness dictates sign. The middle panel shows the ratio of the red and blue galaxy 2-halo terms with the No-Baryon linear model of Eq. (12). The dashed line shows the linear theory model with BAOs. The bottom panel shows the same as the middle only this time we show the effect of including the 1-halo term. The right-hand panel is similar to the left, only we exchange $P_{1\text{-Loop}}$ in the 2-halo term for the `halofit` model [43].

of the bias will also further modify and improve the predictions.

IX. SCALE-DEPENDENT BIAS AT $z > 0$

We have shown that the BAO harmonic series in the power spectrum at ($z = 0$) is affected by nonlinear effects from bias and gravitational evolution. Although naively one might expect that at higher redshift nonlinear effects are less important, this is not necessarily so. First, one must pick a criterion for how to compare things at different redshifts. A natural choice is to use objects of the same number density. In this case, as it is well known, at higher redshifts objects of the same number density are more biased, leading to stronger nonlinear bias effects, even though the dark matter has less nonlinear evolution. Therefore, overall it is not clear *a priori* whether the situation improves or not. Figure 10 shows the halo power spectra at $z = 1$ and $z = 2$ measured from our 8 LR simulations, where the halo samples were harvested so that they would have the same fixed comoving number density as the Bin 1 sample at $z = 0$ (see from Table I). The power spectra analysis was identical to that as described in Sec. III. This figure clearly demonstrates that the nonlinear bias effects that are present at $z = 0$ (Fig. 1), remain present in the high redshift halo samples. In light of this, we anticipate that low mass halo samples at higher redshift, constructed so that $M < M^*(z > 0)$, will likewise show enhanced previrialization ($M^*(z)$ is defined to be the halo mass at which $\sigma(M) = 1$). We reserve further details of this issue for future work.

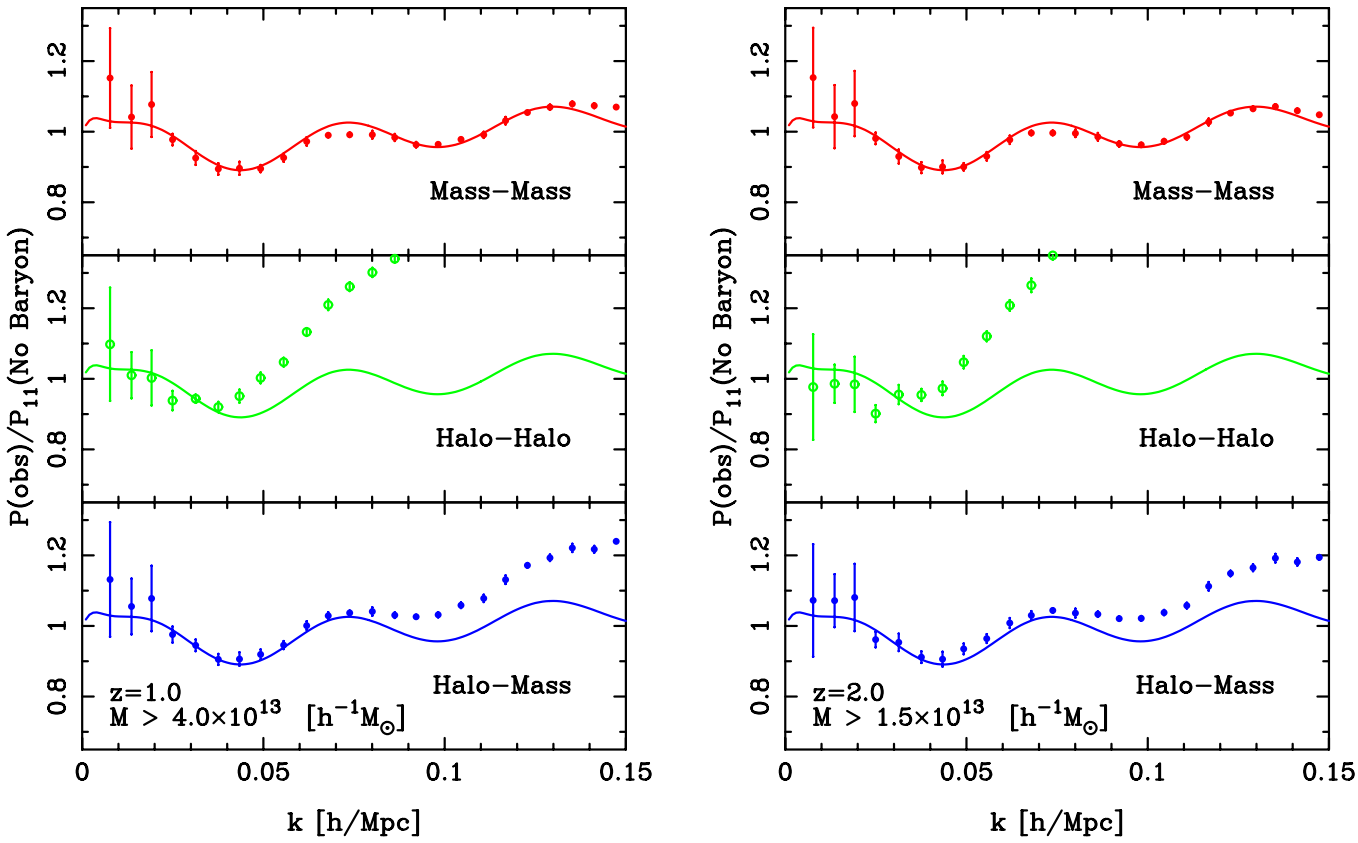

FIG. 10 (color online). Dark matter, halo-halo, and halo-dark matter cross-power spectra at $z = 1$ (left panel) and $z = 2$ (right panel) as a function of wave number. Symbol styles are as in Fig. 1. At both epochs we computed the halo spectra using the same fixed number density of haloes as those in the Bin 1 sample from ($z = 0$): $\bar{n} = 3.43 \times 10^{-5}[h/\mathrm{Mpc}]^3$. Nonlinear mass and bias corrections remain present at the level of 5%–10% in the halo spectra.

X. CONCLUSIONS

In this paper we have explored in detail, through both numerical and analytic means, the scale dependence of the nonlinear dark matter, halo, and galaxy power spectra on very large scales $k < 0.15h$ Mpc^{-1}. For our numerical work we used an ensemble of 20 simulations in boxes of side $512h^{-1}$ Mpc and 8 simulations in boxes of side $\sim 1h^{-1}$ Gpc. Each simulation contained more than 134×10^6 particles. We have found that:

(i) The nonlinear matter power spectrum is suppressed relative to the linear theory by 5%–10% on scales between $0.05 < k/(h\ \mathrm{Mpc}^{-1}) < 0.075$ at the 2-σ level.

(ii) The halo-dark matter cross-power spectrum shows clearly that the bias of halo centers is nonlinear on very large scales. The form of the nonlinearity depends strongly on halo mass: for high mass haloes no previrialization suppression is seen; whereas there is an apparent $\sim$10% suppression of power relative to linear theory for lower mass haloes.

(iii) To make robust statements concerning their large-scale clustering of haloes, it is essential to characterize the shot-noise correction to high precision. For high mass haloes this correction is sub-Poissonian, so the simple and widely used $1/\bar{n}$ model must be inappropriate. Halo exclusion effects lead to a plausible explanation for this phenomenon, which we used to motivate an alternate correction. However further work is required to establish this robustly. In addition the true answer may need to take into account the way in which haloes are identified in simulations.

(iv) The large-scale bias of P^{hh} is not expected to be the same as that of $P^{\delta\mathrm{h}}$ due to nonlinear deterministic bias; this complicates studies of stochastic bias. The difficulty of performing the halo-halo shot-noise correction means we are unable to make a strong statement about the nonequivalence of $b^{\delta\mathrm{h}}$ and b^{hh}.

(v) As wave number increases, low mass haloes are increasingly antibiased and high mass haloes are increasingly positively biased. Therefore, the nonlinear scale dependence of halo bias is not simply due to the nonlinear evolution of the matter fluctuations.

(vi) Baryon acoustic oscillation features in the power spectrum are erased on progressively larger scales as halo mass is increased. In addition, small shifts in

the positions of the higher-order peaks and troughs occur which depend on halo mass.

In the second half of this paper we developed a "physical model" to explain and reproduce these results. The model was constructed within the framework of the halo model and we focused our attention on the clustering of the halo centers. The halo-halo clustering term was carefully propagated into the nonlinear regime using 1-loop perturbation theory and a nonlinear halo bias model. Our model can be summarized as follows: The density field of haloes was assumed to be a function of the local dark matter density field. Under the condition of small fluctuations, it was then expanded as a Taylor series in the dark matter density with nonlinear bias coefficients $b_i(M)$ [16]. The density field was then evolved under 3rd order Eulerian perturbation theory and this provided the 3rd order Eulerian perturbed halo density field. We then used the model to derive the halo-halo and halo-dark matter cross-power spectra up to the 1-loop level. This lead to the following conclusions:

(i) For b_i nonvanishing, the effective bias on very, very large scales for the halo spectra is not simply b_1, but also depends on b_2, b_3 and the variance of fluctuations on scale R. The halo center power spectrum contains a term that corresponds to constant power on very large scales. This implies that as $k \to 0$, halo bias should diverge as $[P_{\rm Lin}]^{-1/2}$. The halo-dark matter cross-power spectrum does not exhibit this behavior. The predicted bias from this statistic approaches a constant value on large scales.

(ii) When evaluated for a realistic cosmological model, with nonlinear bias parameters taken from the Sheth-Tormen mass function, the theory is in broad agreement with numerical simulations for a wide range of halo masses.

(iii) The nonlinear evolution of the BAOs was also examined. The model shows that nonlinear bias and nonlinear mode-mode coupling increasingly damp the BAOs as halo mass is increased. In addition, the positions of the peaks and troughs can be shifted by small amounts which depend on halo mass.

Using the ensemble of simulations we constructed scatter plots of the halo versus dark matter over densities, contained in top-hat spheres of size R (see Appendix B). From these, it was shown that for filter scales $R < 60h^{-1}$ Mpc the bias was indeed nonlinear, and that, while the scatter increased as R decreased, the mean of the relationship did not change until $R < 20h^{-1}$ Mpc. We also examined whether the nonlinear bias parameters derived from the Sheth and Tormen mass function [14,15] provided a reasonable match to the empirical halo bias.

Using semiempirical bias parameters as inputs for the analytic model it was shown that the model well reproduced the scale dependence of the halo-dark matter cross-power spectra in the simulations, and for all bins in halo mass. However, it was only qualitatively able to reproduce the scale dependence of the nonlinear halo bias.

The 1-loop halo center power spectrum was then inserted into the halo-model framework and defined the 1-loop halo-model. This was used to predict the scale dependence of blue and red galaxy power spectra. Plausible models for the blue and red galaxy HODs were used and the results showed complicated scale dependence.

Significant work still remains to be performed for this analytic approach to be sharpened into a tool for precision cosmology. Some possible improvements are: exchanging the 1-loop matter power spectrum for an accurate analytic fitting formula, i.e. after the fashion of `halofit`, but designed purely for large scales; an application of the new renormalized perturbation theory techniques [37,38,82] coupled with the nonlinear bias model should certainly produce better results.

The analytic and numerical results that we have developed here are concerned purely with the clustering in real space. In a subsequent paper we shall extend our analysis to explore the more realistic situation of the scale dependence of dark matter, halo, and galaxy power spectra in redshift space.

When this paper was nearing completion, a preprint appeared [83] with similar calculations of how nonlinear bias changes the power spectrum.

ACKNOWLEDGMENTS

R. E. S. would like to thank Peter Schneider for a very thought provoking discussion that has led to the current paper. We thank Jacek Guzik, Gary Bernstein, Bhuvnesh Jain, and Laura Marian for many useful discussions during this work. We would also like to thank Pat McDonald, Daniel Eisenstein, Eiichiro Komatsu, and Martin White for useful comments on the draft. R. E. S. thanks Joerg Colberg and the Virgo Consortium for providing access to the Hubble Volume and the VLS simulations. R. E. S. thanks CCPP and NYU for their kind hospitality during part of this research. R. S. would like to thank M. Manera for useful discussions on halo exclusion. R. K. S. would like to thank Martin White for many illuminating discussions and the Aspen Center for Physics. We thank M. Crocce and S. Pueblas for help regarding the numerical simulations used here. R. E. S. and R. K. S. both acknowledge support from the National Science Foundation under Grant No. 0520647. R. S. is partially supported by NSF AST-0607747 and NASA NNG06GH21G.

APPENDIX A: HALO DISCRETENESS CORRECTIONS

1. Poisson model

It is necessary to correct the measured dark matter power spectra for shot-noise errors. These arise through approx-

imating the continuous CDM fluid by a point process. If the discretization of the density field obeys a Poisson process, i.e., dark matter particles are placed with probability $\propto \bar{\rho}[1 + \delta(\mathbf{x})]\delta V$, then the "discreteness" correction is [9]:

$$P_{\rm true}(k) = P_{\rm obs}(k) - P_{\rm shot}; \qquad P_{\rm shot} = 1/\bar{n}. \tag{73}$$

Since the number of particles in our simulations is large, 512^3, this correction, on the scales of interest, is insignificant, e.g. $P_{\rm shot}/P(0.1h\ {\rm Mpc}^{-1}) \sim 10^{-3}$. However, one must also correct $P^{\rm hh}$ for discreteness. If the dark matter haloes are also regarded as a Poisson sampling of the smoothed halo density field, then the correction will be the same but using the appropriate number density $\bar{n}_{\rm h}$. In Fig. 11 we show the effect of this standard correction on our halo power spectra and we plot the ensemble of the shot-noise corrected halo power. The negative power values that result at high k demonstrate that this model must not be exactly correct and therefore for accurate measurements it must be modified in some way. We now discuss a possible explanation for this and propose a new shot correction.

2. Halo exclusion effects

As we have seen Poisson sampling must not be exact for haloes, particularly those of large mass. A possible reason is that by using a friends-of-friends algorithm, one is automatically imposing that haloes are never separated by distances smaller than about the sum of their radii, or else they would have been linked as a bigger halo. As a result of this exclusion effect, the two-point correlation function of haloes drops dramatically from a value $\xi^{\rm hh} \gg 1$ at $r \sim r_{\rm e}$ to $\xi^{\rm hh} = -1$ for $r < r_{\rm e}$, where $r_{\rm e}$ is the exclusion radius. This sharp drop of $\xi^{\rm hh}$ has an impact on the large-scale power spectrum, as we now show.

Absent exclusion, the power spectrum would have been

$$P^{\rm hh}(k) = \int_0^\infty \frac{\sin(kr)}{kr}\,\xi^{\rm hh} 4\pi r^2 dr. \tag{A1}$$

However, exclusion effects mean that

$$P^{\rm hh}(k) = \int_{r_{\rm e}}^\infty \frac{\sin(kr)}{kr}\,\xi^{\rm hh} 4\pi r^2 dr - v_{\rm TH}(k), \tag{A2}$$

where $v_{\rm TH}(k) \equiv (4\pi/3) r_{\rm e}^3 W_{\rm TH}(kr_{\rm e})$ with $W_{\rm TH}$ the Fourier transform of a top-hat window in real space. Hence, the difference in power due to exclusion is

$$\Delta P^{\rm hh}(k) = \int_0^{r_{\rm e}} \frac{\sin(kr)}{kr}(1 + \xi^{\rm hh}) 4\pi r^2 dr. \tag{A3}$$

To estimate this, we must model $\xi^{\rm hh}$ at scales smaller than the exclusion imposed by the friends-of-friends definition of a halo. We do so simply by approximating $\xi^{\rm hh}$ by a power-law $\xi^{\rm hh} = \xi_{\rm e}(r/r_{\rm e})^{-\gamma}$ obtained from fitting to the $r \geq r_{\rm e}$ measurements, where $r_{\rm e}$ is the exclusion scale. In this approximation

$$\Delta P^{\rm hh}(k) = v_{\rm TH}(k) + v(k)\xi_{\rm e}, \tag{A4}$$

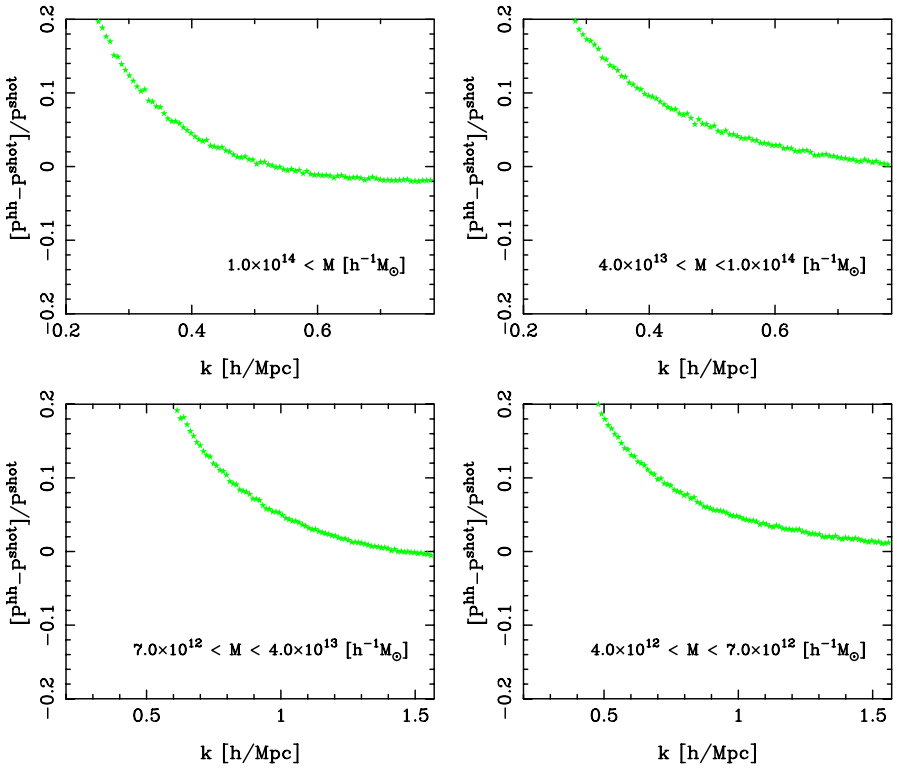

FIG. 11 (color online). The effect of Poisson shot-noise correction on the halo-halo power spectra for the four bins in halo mass.

where, in the large-scale approximation $kr_e \ll 1$,

$$v(k) \simeq \frac{4\pi r_e^3}{3-\gamma} - \frac{2\pi r_e^3}{3(5-\gamma)}(kr_e)^2. \tag{A5}$$

Setting $\gamma = 0$ gives v_{TH} in the same limit. Thus, we see that exclusion makes the halo power spectrum *smaller* by the amount given by Eq. (A4). In contrast, Poisson shot noise makes the power *larger* by $1/\bar{n}_h$. If Poisson noise is subtracted from halo power spectra in simulations, then the result becomes negative at high k, and so it may be that adding back the power lost to exclusion will make the power positive again. This is our procedure. Note that the noise in Eq. (A4) *is not white*.

As a final note we reemphasize that all of these troubling issues may, to a certain extent, be neatly side stepped, if we measure the halo-dark matter cross-power spectrum. The clear advantage of this approach is that the shot-noise is dramatically reduced (there are many more particles than haloes) and exclusion no longer plays a role.

APPENDIX B: MEASURING THE NONLINEAR BIAS PARAMETERS

The accuracy of 1-loop halo PT depends on the accuracy of the halo bias parameters b_1, b_2, and b_3. Figure 4 shows these parameters derived from the conditional Sheth and Tormen mass function [15]. There are a number of ways to test the accuracy of the bias parameters. The most direct is to smooth the halo and mass fields with a filter of scale R, and to then plot $\delta^h(x|R)$ versus $\delta(x|R)$ in the smoothed fields (e.g. [68,84]). From the resulting scatter plot, one then directly fits for the parameters b_i up to some order, subject to the constraint that $\langle\delta^h\rangle = \langle\delta\rangle = 0$.

Figure 12 shows such scatter plots for the four bins in halo mass described earlier (Table I). In all cases, unlike elsewhere in the paper, the fields were filtered with a ''top-hat'' window function. Solid lines show results for four filter scales $R_{TH} = \{20, 30, 40, 50\}h^{-1}$ Mpc. The upper and lower dotted lines show the 1-σ errors about the mean relation (solid lines). (Smoothing with a Gaussian filter instead does not significantly change the mean, but does slightly change the scatter around the mean relation.) The figure shows that, above a certain scale, $\langle\delta^h|\delta\rangle$ defines a universal curve which is independent of R; it is this curve which the bias coefficients are supposed to describe. The figure also shows that the scatter around this mean curve decreases as R increases. The assumption that bias is deterministic is equivalent to assuming that this scatter, this stochasticity, is negligible. Clearly, this is a reasonable approximation only for large smoothing scales R, and R must be bigger for the rarer, more massive haloes before the bias can be called deterministic.

The main problem with this approach is that, when R is large, then the distribution of δ becomes sharply peaked about its mean value (zero), so estimating the higher-order bias coefficients becomes difficult—only the linear bias term can be reliably measured. In effect, determination of the bias coefficients corresponds to fitting a polynomial to these mean curves, and the best-fitting coefficients will be correlated. The results of this exercise are tabulated in Table II, which also shows the values of b_i predicted from the Sheth-Tormen mass function. Some of the discrepancy is a consequence of the fact that the Sheth-Tormen mass function underpredicts the abundance of high mass haloes in the HR and LR simulations by up to 20% (see [40] for an explanation as to why this happens). But note that, because of the correlation between the fitted coefficients, the discrepancy with the theory values is difficult to assess. The solid thick line in the figure shows the mean bias relation derived from the Sheth-Tormen mass function.

In light of these issues we use the following prescription when generating the theory curves: b_1 coefficients are to be measured directly from the data as described in Sec. III B and the parameters b_2 and b_3 are to be derived through computing the following integrals over the relevant bin width:

$$\bar{b}_i(M) = \frac{1}{\bar{n}(M_1, M_2)} \int_{M_1}^{M_2} dM n(M) b_i(M), \tag{B1}$$

where $n(M)$ and $b_i(M)$ are the Sheth and Tormen mass function and bias parameters. We shall refer to this approach as the semiempirical method. It shall be left to our future work to provide a more self-consistent solution to this problem.

APPENDIX C: EULERIAN PT

1. Real-space kernels

The growth of density inhomogeneities in an expanding universe may be explored in the single stream approximation using the Eulerian fluid equations. In Fourier space the equations governing the evolution of the fluctuations to the density ($\delta(\mathbf{k}, t)$) and divergence of the peculiar velocity field ($\theta(\mathbf{k}, t) \equiv \nabla \cdot \mathbf{v}$) are written [10]:

$$\frac{\partial\delta(\mathbf{k}, t)}{\partial t} + \theta(\mathbf{k}, t) = -\int \frac{d^3q_1 d^3q_2}{(2\pi)^3} \times [\delta^D(\mathbf{k})]_2 \alpha(\mathbf{q}_1, \mathbf{q}_2)\theta(\mathbf{q}_1, t)\delta(\mathbf{q}_2, t), \tag{C1}$$

$$\frac{\partial\theta(\mathbf{k}, t)}{\partial t} + H(a)\theta(\mathbf{k}, t) + \frac{3}{2}\Omega_m H^2(t)\delta(\mathbf{k}, t) = -\int \frac{d^3q_1 d^3q_2}{(2\pi)^3} [\delta^D(\mathbf{k})]_2 \beta(\mathbf{q}_1, \mathbf{q}_2)\theta(\mathbf{q}_1, t)\theta(\mathbf{q}_2, t), \tag{C2}$$

where

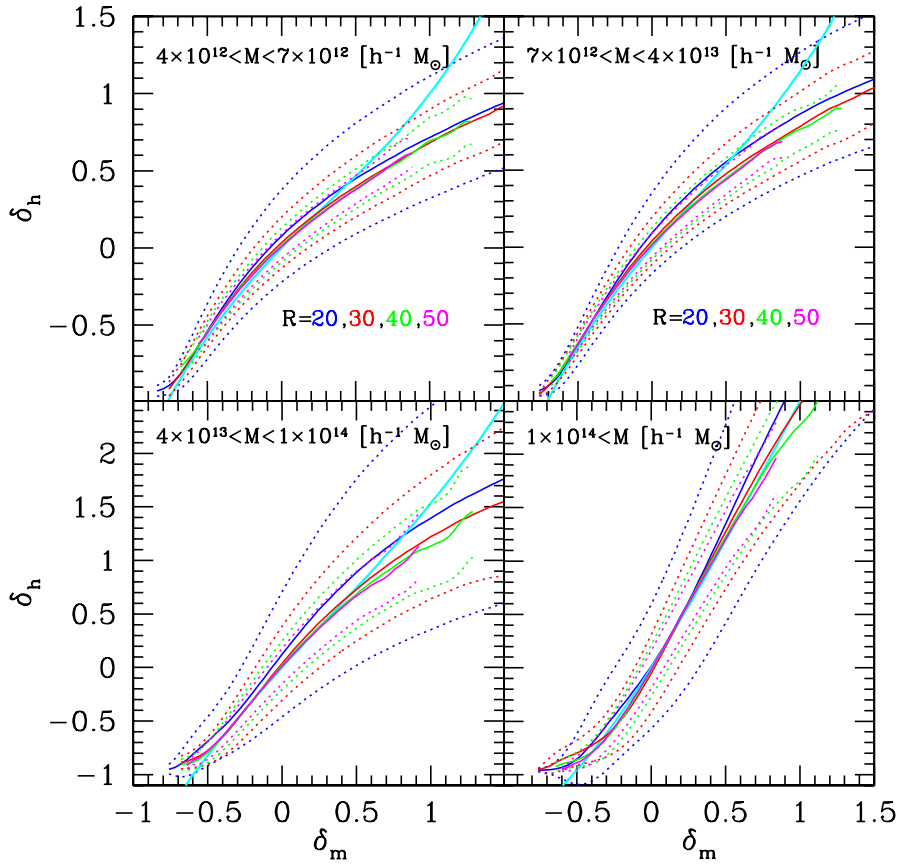

FIG. 12 (color online). Scatter plot of halo number over density vs the over density of dark matter for four bins in halo mass. The fluctuations were measured in top-hat spheres of radii $R_{\rm TH} = \{20, 30, 40, 50\}h^{-1}$ Mpc. The means and 1-sigma errors measured from the ensemble are denoted by the solid, dashed, dot-dashed, and dotted lines, respectively. The solid thick line shows the predictions from the Sheth and Tormen model. The thick triple dot-dashed lines show the results from the cubic fit in δ as described in the text.

$$\alpha_{i,j} \equiv \alpha(\mathbf{q}_i, \mathbf{q}_j) \equiv \frac{\mathbf{k}\cdot\mathbf{q}_i}{q_i^2};$$
$$\beta_{i,j} \equiv \beta(\mathbf{q}_i, \mathbf{q}_j) \equiv \frac{k^2(\mathbf{q}_i\cdot\mathbf{q}_j)}{2q_i^2 q_j^2}; \qquad \mathbf{k} = \mathbf{q}_i + \mathbf{q}_j. \tag{C3}$$

As shown in [10], for the case of the Einstein-de Sitter model the density and velocity divergence fields may be expanded as a perturbation series and the solutions at each order may then be written down in terms of the density and velocity perturbations from all lower orders: e.g.

$$\delta(\mathbf{k}) = \sum_{n=1}^{\infty} D_1^n(a)\delta_n(\mathbf{k});$$
$$\delta_n(\mathbf{k}) = \int \frac{\prod_{i=1}^n \{d^3k_i\delta_1(\mathbf{k}_i)\}}{(2\pi)^{3n-3}} [\delta^D(\mathbf{k})]_n F_n^{(s)}(\mathbf{k}_1, \ldots, \mathbf{k}_n), \tag{C4}$$

$$\theta(\mathbf{k}) = H(a)f(a)\sum_{n=1}^{\infty} D_1^n(a)\theta_n(\mathbf{k});$$
$$\theta_n(\mathbf{k}) = \int \frac{\prod_{i=1}^n \{d^3k_i\delta_1(\mathbf{k}_i)\}}{(2\pi)^{3n-3}} [\delta^D(\mathbf{k})]_n G_n^{(s)}(\mathbf{k}_1, \ldots, \mathbf{k}_n), \tag{C5}$$

where $H(a)$ is the dimensionless Hubble parameter, $D_1(a) = a$ is the linear growth factor, and $f(a) = d\log D/d\log a \approx \Omega_m^{5/9}$ gives the velocity growth suppression factor. The functions $F_n^{(s)}$ and $G_n^{(s)}$ are the PT kernels for δ and θ symmetrized in all of their arguments, respectively. The notation $[\delta^D(\mathbf{k})]_n = \delta^D(\mathbf{k} - \mathbf{q}_1 - \cdots - \mathbf{q}_n)$ was adopted. The first three symmetrized density kernels are:

$$F_1^{(s)}(\mathbf{q}) = 1; \tag{C6}$$

$$F_2^{(s)}(\mathbf{q}_1, \mathbf{q}_2) = \tfrac{5}{14}[\alpha_{1,2} + \alpha_{2,1}] + \tfrac{2}{7}\beta_{1,2}; \tag{C7}$$

$$F_3^{(s)}(\mathbf{q}_1, \mathbf{q}_2, \mathbf{q}_3) = \tfrac{7}{54}[F_{1,2}^{(s)}\alpha_{3,12} + F_{2,3}^{(s)}\alpha_{1,23} + F_{3,1}^{(s)}\alpha_{2,31} + G_{1,2}^{(s)}\alpha_{12,3} + G_{2,3}^{(s)}\alpha_{23,1} + G_{3,1}^{(s)}\alpha_{31,2}] + \tfrac{2}{27}[G_{1,2}^{(s)}\beta_{12,3} + G_{2,3}^{(s)}\beta_{23,1} + G_{3,1}^{(s)}\beta_{31,2}]. \tag{C8}$$

The first three symmetrized velocity divergence PT kernels are:

$$G_1^{(s)}(\mathbf{q}) = 1; \tag{C9}$$

$$G_2^{(s)}(\mathbf{q}_1,\mathbf{q}_2) = \tfrac{3}{14}[\alpha_{1,2}+\alpha_{2,1}] + \tfrac{4}{7}\beta_{1,2}; \tag{C10}$$

$$\begin{aligned} G_3^{(s)}(\mathbf{q}_1,\mathbf{q}_2,\mathbf{q}_3) = {} & \tfrac{1}{18}[F_{1,2}^{(s)}\alpha_{3,12} + F_{2,3}^{(s)}\alpha_{1,23} + F_{3,1}^{(s)}\alpha_{2,31} \\ & + G_{1,2}^{(s)}\alpha_{12,3} + G_{2,3}^{(s)}\alpha_{23,1} + G_{3,1}^{(s)}\alpha_{31,2}] \\ & + \tfrac{2}{9}[G_{1,2}^{(s)}\beta_{12,3} + G_{2,3}^{(s)}\beta_{23,1} + G_{3,1}^{(s)}\beta_{31,2}], \end{aligned} \tag{C11}$$

where we have adopted the compact notation

$$\begin{aligned} F_{i_1,\ldots,i_n}^{(s)} &\equiv F_n^{(s)}(\mathbf{q}_{i_1},\ldots,\mathbf{q}_{i_n}); \\ G_{i_1,\ldots,i_n}^{(s)} &\equiv G_n^{(s)}(\mathbf{q}_{i_1},\ldots,\mathbf{q}_{i_n}) \end{aligned} \tag{C12}$$

and

$$\begin{aligned} \alpha_{i_1\ldots i_n,j_1\ldots j_m} &\equiv \alpha(\mathbf{q}_{i_1}+\cdots+\mathbf{q}_{i_n},\mathbf{q}_{j_1}+\cdots+\mathbf{q}_{j_m}); \\ \beta_{i_1\ldots i_n,j} &\equiv \beta(\mathbf{q}_{i_1}+\cdots+\mathbf{q}_{i_n},\mathbf{q}_j). \end{aligned} \tag{C13}$$

Exact analytic solutions for arbitrary cosmological models have not yet been found. However, as was shown in [85], under the assumption that $D_n(a) \propto [D_1(a)]^n$ and $f(\Omega) \approx \Omega_m^{0.5}$, the solutions are identical to the Einstein-de Sitter solutions, but the growth factors are changed to those for the particular cosmological model in question. All other changes are small corrections [10].

2. Evaluation of 1-loop expressions

Some care is required in the numerical evaluation of the halo-PT expressions because fine cancellations can occur between negative and positive terms. The approach that we adopt throughout this paper can be demonstrated through the following example. Consider the 1-loop power spectrum for CDM given by Eq. (48). The PT corrections P_{13} and P_{22} may be analytically developed up to the following points:

$$\begin{aligned} P_{13}(k) &= 6P_{11}(k)\int\frac{dq}{(2\pi)^3}q^2P_{11}(q)\int d\hat{\mathbf{q}}F_3(\mathbf{k},\mathbf{q},-\mathbf{q}) \\ &= \frac{P_{11}(k)k^3}{252(2\pi)^2}\int_0^\infty dx\,x^2P_{11}(xk)\Big\{-42x^2+100 \\ &\quad -\frac{158}{x^2}+\frac{12}{x^4}+\frac{3}{x}(1-x^2)^3(7x^2+2) \\ &\quad \times\log\left[\frac{x+1}{|x-1|}\right]\Big\}; \end{aligned} \tag{C14}$$

$$\begin{aligned} P_{22}(k) &= 2\int\frac{d^3q}{(2\pi)^3}P_{11}(q)P_{11}(|\mathbf{k}-\mathbf{q}|)[F_2(\mathbf{q},\mathbf{k}-\mathbf{q})]^2 \\ &= 2\int_0^\infty\frac{dq}{(2\pi)^2}q^2P_{11}(q)\int_{-1}^1 d\mu P_{11}(k\psi(x,\mu)) \\ &\quad \times\left\{\frac{5}{7}+\frac{1}{2}\frac{\mu-x}{\psi(x,\mu)}\left[\frac{x}{\psi(x,\mu)}+\frac{\psi(x,\mu)}{x}\right]\right. \\ &\quad \left.+\frac{2}{7}\left[\frac{\mu-x}{\psi(x,\mu)}\right]^2\right\}^2, \end{aligned} \tag{C15}$$

where $x = q/k$ and where $\psi^2(x,\mu) = 1+x^2-2x\mu$. If the P_{13} integral is truncated on large and small scales to inhibit infrared and ultraviolet divergences, as may occur for some power spectra, then identical constraints must also be placed on the $P_{22}(k)$. Explicitly, if we adopt

$$P(q) = 0 \quad \text{for} \begin{cases} k < k_{\rm fun} \\ k > k_{\rm cut} \end{cases},$$

then the angular integral for P_{22} must necessarily have the new limits

$$\begin{aligned} &\int_{-1}^1 d\mu \to \int_{\mu_1}^{\mu_2}; \\ &\mu_2 = \min[1,\sqrt{(k^2+q^2-k_{\rm cut}^2)/2kq}]; \\ &\mu_1 = \max[-1,\sqrt{(k^2+q^2-k_{\rm fun}^2)/2kq}]. \end{aligned} \tag{C16}$$

Lastly, the particular values for the limits $k_{\rm fun}$ and $k_{\rm cut}$ were selected so that variance integrals, $\sigma^2(R)$, would be convergent within the finite range.

[1] E. Hawkins *et al.*, Mon. Not. R. Astron. Soc. **346**, 78 (2003).
[2] D. J. Eisenstein *et al.*, Astrophys. J. **633**, 560 (2005).
[3] M. Tegmark *et al.*, Astrophys. J. **606**, 702 (2004).
[4] S. Cole *et al.*, Mon. Not. R. Astron. Soc. **362**, 505 (2005).
[5] M. Tegmark *et al.*, Phys. Rev. D **74**, 123507 (2006).
[6] W. Percival *et al.*, astro-ph/0608635.
[7] W. Percival *et al.*, astro-ph/0608636.
[8] D. Spergel *et al.*, astro-ph/0603449.
[9] P. J. E. Peebles, *The Large-scale Structure of the Universe* (Princeton University, Princeton, NJ, 1980).
[10] F. Bernardeau, S. Colombi, E. Gaztañga, and R. Scoccimarro, Phys. Rep. **367**, 1 (2002).
[11] S. Cole and N. Kaiser, Mon. Not. R. Astron. Soc. **237**, 1127 (1989).
[12] H.-J. Mo and S. D. M. White, Mon. Not. R. Astron. Soc. **282**, 347 (1996).
[13] H.-J. Mo, Y.-P. Jing, and S. D. M. White, Mon. Not. R. Astron. Soc. **284**, 189 (1997).
[14] R. K. Sheth and G. Tormen, Mon. Not. R. Astron. Soc.

308, 119 (1999).
[15] R. Scoccimarro, R. K. Sheth, L. Hui, and B. Jain, Astrophys. J. **546**, 20 (2001).
[16] J. Fry and E. Gaztañaga, Astrophys. J. **425**, 1 (1993).
[17] Several broad classes of the bias model may be defined: local [86] and nonlocal [66,87–90]; linear or nonlinear [16,19,20,73,91–93]; and deterministic or stochastic [35,94]. With the exception of stochastic, local, linear biasing, all these prescriptions result in some nontrivial degree of scale dependence. Note that when weakly nonlinear scales are discussed, as we do in this paper, it may not be entirely consistent to neglect nonlocality, which could potentially alter the predictions we present. Nonlocal bias can be looked for in observations by using higher-order statistics [81,95]. However, we may take comfort in the fact that there is always a strong correlation between haloes and dark matter, since the former are built from the latter.
[18] S. D. M. White and M. Rees, Mon. Not. R. Astron. Soc. **183**, 341 (1978).
[19] A. J. Benson, S. Cole, C. S. Frenk, C. Baugh, and C. Lacey, Mon. Not. R. Astron. Soc. **311**, 793 (2000).
[20] J. A. Peacock and R. E. Smith, Mon. Not. R. Astron. Soc. **318**, 1144 (2000).
[21] U. Seljak, Mon. Not. R. Astron. Soc. **318**, 203 (2000).
[22] A. Berlind and D. Weinberg, Astrophys. J. **575**, 587 (2002).
[23] A. Meiksin, M. White, and J. A. Peacock, Mon. Not. R. Astron. Soc. **304**, 851 (1999).
[24] H.-J. Seo and D. Eisenstein, Astrophys. J. **598**, 720 (2003).
[25] H.-J. Seo and D. Eisenstein, Astrophys. J. **633**, 575 (2005).
[26] M. White, Astropart. Phys. **24**, 334 (2005).
[27] E. Huff, A. E. Schulz, M. White, D. J. Schlegel, and M. Warren, Astropart. Phys. **26**, 351 (2007).
[28] M. Crocce and R. Scoccimarro (unpublished).
[29] D. Jeong and E. Komatsu, Astrophys. J. **651**, 619 (2006).
[30] J. Guzik, G. Bernstein, and R. E. Smith, astro-ph/0605594.
[31] D. J. Eisenstein, H.-J. Seo, E. Sirko, and D. Spergel, astro-ph/0604362.
[32] D. J. Eisenstein, H.-J. Seo, and M. White, astro-ph/0604361.
[33] U. Seljak and M. Zaldarriaga, Astrophys. J. **469**, 437 (1996).
[34] N. Padmanabhan *et al.*, astro-ph/0605302.
[35] R. Scherrer and D. Weinberg, Astrophys. J. **504**, 607 (1998).
[36] U. Seljak, Mon. Not. R. Astron. Soc. **325**, 1359 (2001).
[37] M. Crocce and R. Scoccimarro, Phys. Rev. D **73**, 063519 (2006).
[38] M. Crocce and R. Scoccimarro, Phys. Rev. D **73**, 063520 (2006).
[39] V. Springel, Mon. Not. R. Astron. Soc. **364**, 1105 (2005).
[40] M. Crocce, S. Pueblas, and R. Scoccimarro, Mon. Not. R. Astron. Soc. **373**, 369 (2006).
[41] M. S. Warren, K. Abazajian, D. E. Holz, and L. Teodoro, Astrophys. J. **646**, 881 (2006).
[42] The dark matter particles/halo centers were assigned to a regular cubical grid using a fourth-order interpolation scheme, and each point on the grid was given equal weight. The FFT of the gridded density field was then computed. Each resulting Fourier mode was corrected for convolution with the grid by dividing by the Fourier transform of the mass assignment window function. The power spectra on scale k_l are then estimated by performing the following sums,

$$\hat{P}^{ij}(k_l) = \frac{1}{M}\sum_{l=1}^{M} |\delta^i(\mathbf{k}_l)(\delta^j(\mathbf{k}_l))^*|^2,$$

where M are the number of Fourier modes in a spherical shell in k-space of thickness Δk, and $*$ denotes complex conjugation.
[43] R. E. Smith, J. A. Peacock, A. Jenkins, S. D. M. White, C. S. Frenk, F. R. Pearce, P. A. Thomas, G. Efstathiou, and H. M. P. Couchman, Mon. Not. R. Astron. Soc. **341**, 1311 (2003).
[44] J. R. Bond and G. Efstathiou, Astrophys. J. **285**, L45 (1984).
[45] The procedure was also performed separately for the no-baryon model spectrum; this was done in order for ratios to be taken.
[46] W. Percival *et al.*, Mon. Not. R. Astron. Soc. **327**, 1297 (2001).
[47] V. Springel *et al.*, Nature (London) **435**, 629 (2005).
[48] A. Cooray and R. K. Sheth, Phys. Rep. **372**, 1 (2002).
[49] J. Neyman and E. Scott, Astrophys. J. **116**, 144 (1952).
[50] P. J. E. Peebles, Astron. Astrophys. **32**, 197 (1974).
[51] J. McClelland and J. Silk, Astrophys. J. **217**, 331 (1977).
[52] R. Scherrer and E. Bertschinger, Astrophys. J. **381**, 349 (1991).
[53] R. K. Sheth and B. Jain, Mon. Not. R. Astron. Soc. **285**, 231 (1997).
[54] I. Zehavi *et al.*, Astrophys. J. **608**, 16 (2004).
[55] X. Yang, H.-J. Mo, Y. P. Jing, F. C. van den Bosch, and Y. Chu, Mon. Not. R. Astron. Soc. **350**, 1153 (2004).
[56] I. Zehavi *et al.*, Astrophys. J. **630**, 1 (2005).
[57] R. Skibba, R. K. Sheth, A. Connolly, and R. Scranton, Mon. Not. R. Astron. Soc. **369**, 68 (2006).
[58] U. Abbas and R. K. Sheth, Mon. Not. R. Astron. Soc. **372**, 1749 (2006).
[59] R. E. Smith and P. I. R. Watts, Mon. Not. R. Astron. Soc. **360**, 203 (2005).
[60] R. E. Smith, P. I. R. Watts, and R. K. Sheth, Mon. Not. R. Astron. Soc. **365**, 214 (2006).
[61] C.-P. Ma and J. Fry, Astrophys. J. **543**, 503 (2000).
[62] R. K. Sheth, L. Hui, A. Diaferio, and R. Scoccimarro, Mon. Not. R. Astron. Soc. **325**, 1288 (2001).
[63] X. Yang, H.-J. Mo, and F. van den Bosch, Mon. Not. R. Astron. Soc. **339**, 1057 (2003).
[64] A. E. Evrard, T. J. MacFarland, H. M. P. Couchman, J. M. Colberg, N. Yoshida, S. D. M. White, A. Jenkins, C. S. Frenk, F. R. Pearce, J. A. Peacock, and P. A. Thomas, Astrophys. J. **573**, 7 (2002).
[65] J. Tinker, D. Weinberg, Z. Zheng, and I. Zehavi, Astrophys. J. **631**, 41 (2005).
[66] P. Catelan, S. Matarrese, and C. Porciani, Astrophys. J. **502**, L1 (1998).
[67] Y.-P. Jing, Astrophys. J. **503**, L9 (1998).
[68] R. K. Sheth and G. Lemson, Mon. Not. R. Astron. Soc. **304**, 767 (1999).
[69] Y.-P. Jing, Astrophys. J. **515**, L45 (1999).
[70] A. Kravtsov and A. Klypin, Astrophys. J. **520**, 437 (1999).

[71] T. Hamana, N. Yoshida, Y. Suto, and A. Evrard, Astrophys. J. **561**, L143 (2001).
[72] U. Seljak and M. Warren, Mon. Not. R. Astron. Soc. **355**, 129 (2004).
[73] A. F. Heavens, S. Matarrese, and L. Verde, Mon. Not. R. Astron. Soc. **301**, 797 (1998).
[74] A. Taruya, Astrophys. J. **537**, 37 (2000).
[75] J. Navarro, C. S. Frenk, and S. D. M. White, Astrophys. J. **490**, 493 (1997).
[76] R. K. Sheth and A. Diaferio, Mon. Not. R. Astron. Soc. **322**, 901 (2001).
[77] G. Kauffmann, J. M. Colberg, A. Diaferio, and S. D. M. White, Mon. Not. R. Astron. Soc. **303**, 188 (1999).
[78] A. Kravtsov, A. Berlind, R. Wechsler, A. Klypin, S. Gottlober, B. Allgood, and J. Primack, Astrophys. J. **609**, 35 (2004).
[79] A. Berlind, D. Weinberg, A. J. Benson, C. M. Baugh, S. Cole, R. Davé, C. S. Frenk, A. Jenkins, N. Katz, and C. G. Lacey, Astrophys. J. **593**, 1 (2003).
[80] Z. Zheng, A. Berlind, D. Weinberg, A. J. Benson, C. M. Baugh, S. Cole, R. Davé, C. S. Frenk, N. Katz, and C. G. Lacey, Astrophys. J. **633**, 791 (2005).
[81] H. Feldman, J. Frieman, J. N. Fry, and R. Scoccimarro, Phys. Rev. Lett. **86**, 1434 (2001).
[82] P. McDonald, astro-ph/0606028 [Phys. Rev. D (to be published)].
[83] P. McDonald, Phys. Rev. D **74**, 103512 (2006); **74**, 129901(E) (2006).
[84] R. Casas-Miranda, H. J. Mo, R. K. Sheth, and G. Boerner, Mon. Not. R. Astron. Soc. **333**, 730 (2002).
[85] R. Scoccimarro, S. Colombi, J. N. Fry, J. A. Frieman, E. Hivon, and A. Melott, Astrophys. J. **496**, 586 (1998).
[86] P. Coles, Mon. Not. R. Astron. Soc. **262**, 1065 (1993).
[87] N. Kaiser, Astrophys. J. **284**, L9 (1984).
[88] A. Dekel and M. Rees, Nature (London) **326**, 455 (1987).
[89] P. Catelan, C. Porciani, and M. Kamionkowski, Mon. Not. R. Astron. Soc. **318**, L39 (2000).
[90] T. Matsubara, Astrophys. J. **525**, 543 (1999).
[91] R. Cen and J. Ostriker, Astrophys. J. **399**, L113 (1992).
[92] R. Mann, J. A. Peacock, and A. F. Heavens, Mon. Not. R. Astron. Soc. **293**, 209 (1998).
[93] R. Cen and J. Ostriker, Astrophys. J. **538**, 83 (2000).
[94] A. Dekel and O. Lahav, Astrophys. J. **520**, 24 (1999).
[95] J. A. Frieman and E. Gaztañaga, Astrophys. J. **425**, 392 (1994).